UNIVERSITEIT UTRECHT

DEBYE INSTITUTE FOR NANOMATERIALS SCIENCE

CENTER FOR EXTREME MATTER AND EMERGENT PHENOMENA

NANOPHOTONICS SECTION

Experiments on Ablation of Dielectrics on Gold, and Water

Author:
M. Scholten BSc.

Supervisor:
Dr. D. van Oosten

January 8, 2016

Abstract

We performed ablation on both an air-water interface and a gold-silica-air interface. Pulses with a duration of $160\,\mathrm{fs}$ were shot at the materials, with fluences ranging from $0.2\,\mathrm{mJ\,cm^{-2}}$ up to $0.35\,\mathrm{J\,cm^{-2}}$. This was done to study the self-reflectivity.

According to existing theory the reflectivity of water should not significantly change in this fluence regime. We measure however an increase of 0.0023, around a fluence of $1\,\mathrm{mJ\,cm^{-2}}$, after which the reflectivity stays at this constant at the higher value.

When performing the measurement on the gold with a thin nano-layer of silica, we witness ablation at fluences around the ablation threshold of gold, but far below that of silica. The addition of a thin layer of silica decreases the addition with approximately 40%. Increasing the thickness of the layer will lead to an increase again of the ablation threshold.

The self-reflectivity of the samples resemble those of gold, but see a steeper decline. We developed a simple model, assuming no non-linear behaviour of the silica. We will present evidence suggesting penetration of hot electrons from the gold in the silica.

Contents

1 Introduction

1.1 Theoretical introduction

After the first laser was created in 1960 [1], the use of it for laser ablation was quickly acknowledged [2,3]. After this it became a rapidly expanding field, by 1968 it had already reached the realm of biology [4]. At present, laser ablation plays an increasing role in society, mainly in, but not limited to nanofabrication, medicine and industry.

Laser ablation is a broad subject which includes any removal of material of a sample with the use of a laser beam. Usually the beam is focused to decrease the spot size, thereby increasing the fluence. The properties of the laser can differ over a whole range. For different parameters however, different physical processes can be responsible for the removal. For low fluence, high repetition rates and high pulse lengths(or even continuous operation) melting and subsequent evaporation will be the dominant mechanism. The shorter the pulse is, the more violent the process. If the fluences are high enough, a plasma can even be created [5,6].

The use of lasers for material removal has numerous advantages. First of all no chemicals have to be used, so there is no pre- or postprocessing necessary, nor is a special chemical setup. Sometimes it is the removed material which is needed [7], in which case you need a mechanism which only removes and disperses the material, but does nothing else. Laser ablation provides the solution for this, it is then called pulsed laser deposition [8]. But the most important benefits is the low amount of damage done to the rest of the material. Since a laser pulse is by definition localized in space, only through diffusion it can influence the rest of the material. The shorter the pulse becomes, the less time is available for diffusion, limiting the possible area effected. It is however possible that the surrounding material melts and solidifies again without loss of structure [9]. With the use of femtosecond pulses, it is even possible to reach sub-diffraction resolution [10]. This is one of the reasons femtosecond pulses are used to micromachine all kinds of materials [11–17]

Femtosecond pulses have high enough peak energy to ionize the material. For metals the dominant process is free-carrier absorption. Since semiconductors and dielectrics lack a high initial density of free carriers, photon absorption and impact ionization dominate the interaction [10]. In both cases a high-density electron-hole plasma will be created, which destroys the covalent bonds, creating a repulsive potential between the atoms [18–20]. The energy relaxation of electrons is caused by electron phonon-scattering. This happens however on a picosecond timescale. Considering that the melting happens faster then the actual heating of the material, this is called non-thermal melting [21,22]. Since both for metals and non-metals a plasma is formed, and since plasmas have a very high absorbence, femtosecond pulses can not penetrate very deeply into the material, usually maximally $150\,\mathrm{nm}$ [10].

Water is the most abundant material on the surface of the Earth, yet there has not been many measurements of the short pulse response. Silicon has been the favourite of the ablation community, due to its numerous applications, such as direct laser writing of photonic devices [13]. The liquid nature of water makes it harder to study the effects, since there is no permanent trace of the ablation. However since it is also one of the most used solvents in the world, we find it a material worth studying.

Metals usually have a low ablation threshold compared to dielectrics. A thin layer of silica on top of a layer of gold will transmit a substantial fluence to reach the silica-gold interface. So we can safely expect that ablation will occur there. But this does not tell us what will happen, since the gold is separated form the air by a (possibly still solid) layer of glass. Every phase of the ablation process can in principle be affected by the presence of the silica layer. Dependant on the thickness of the layer, absorbance of the layer can change [23], thereby altering the influence. This might result in a material which is easier to micromachine then existing materials.

For this work we use single $800\,\mathrm{nm}$ pulses with a a pulse length of $160\,\mathrm{fs}$. We use a high NA-objective to focus these pulses to a spotsize of approximately $1\,\mathrm{\mu m}^2$. Two different samples were investigated. One consists of demineralized water, the other of a thin layers of silica of increasing thickness on top of a layer of gold. The reflectivity was measured for different fluences.

1.2 Outline thesis

First in section 2 the theory behind ablation and non-linear optics is introduced. Further the models used to explain the behaviour of these specific materials are discussed in this section. In section 3, the setup, build during this research year, is discussed. Also the samples and the mode of operations is included here. Then section 4 describes the results of the measurements. First the ablation of water, followed by the ablation of silica films on gold. Subsequently the conclusions are drawn from this in section 5.

2 Theory

Since what we eventually measure is the reflected light, we need to model what happens to the reflectivity under ablation conditions. This behaviour is incorporated in the refractive index, for which the dielectric function is needed. In section 2.1 we will discuss the Drude model, the simplest model describing the optical properties of a free electron gas.

For the thin layers of glass on gold, we also need to take the interference within the glass into account. We do this by the application of the Transfer matrix model. This will be explained in section 2.2. One of the input parameters of the Transfer matrix model is the refractive index of gold. We will derive the refractive index in section 2.3 with the use of the Drude model. Finally, in section 2.4 we will calculate the carrier density of a water plasma. This is one of the parameters we need to calculate the dielectric function with the use of the Drude model.

2.1 Drude model

The Drude model, first proposes by Paul Drude in 1900 [24] assumes the equation of motion of an electron is

$$\frac{d\vec{p}}{dt} = \vec{F}_{L,\text{ext}} - \frac{\vec{p}}{\tau}. \tag{2.1}$$

Here $\vec{p}$ is the momentum of the electron and τ is the average time between two collisions after which, it is assumed, the orientational information of the momentum is lost and thus the average momentum is zero. This means on average $\Delta\vec{p} = -\vec{p}$. Here $\vec{F}_{L,\text{ext}}$ is the external Lorentz force on the particle, which under our conditions equals

$$\vec{F}_{L,ext} = -e\vec{E}\mathrm{e}^{-i\omega t}, \tag{2.2}$$

where ω is the frequency of the incoming light, and $\vec{E}$ the (complex) amplitude of the electric field. Solving equations 2.1 and 2.2 gives the solution for the momentum of electrons

$$\vec{p}(t) = \frac{-e\vec{E}\mathrm{e}^{-i\omega t}}{1/\tau - i\omega}. \tag{2.3}$$

Given a free electron density of N, the current density becomes

$$\vec{J} = -\frac{Ne\vec{p}}{m}. \tag{2.4}$$

If we plug equation 2.3 into equation 2.4 and the apply Ohm's law we obtain the conductivity

$$\sigma(\omega) = \frac{Ne^2\tau}{m(1 - i\omega\tau)}. \tag{2.5}$$

3

If we combine that with the relation between the conductivity and the dielectric function,

$$\epsilon(\omega) = 1 + \frac{i\sigma(\omega)}{\epsilon_0\omega} \tag{2.6}$$

we end up with,

$$\epsilon(\omega) = 1 - \left(\frac{\omega_p}{\omega}\right)^2 \frac{1}{1 + \frac{i}{\omega\tau}} \tag{2.7}$$

where $\omega_p = \sqrt{\frac{Ne^2}{\epsilon_0 m}}$ is called the plasma frequency. For a real material, which already has a dielectric function due to the bound electron resonances at higher frequencies, this becomes

$$\epsilon_{\mathrm{m}}(\omega) = \epsilon_{\mathrm{um}} - \left(\frac{\omega_p}{\omega}\right)^2 \frac{1}{1 + \frac{i}{\omega\tau}} \tag{2.8}$$

where ϵ_{um} and ϵ_{m} refer to the unexcited and exited material respectively. Note however that gold the dielectric function already has a Drude contribution.

2.2   Transfer matrix method

The Transfer matrix method (TMM) describes how electromagnetic waves of a specific wavevector travel through a layered material [25]. It exploits the fact that while there are discontinuities at a boundary, both the electric field and its derivative in the direction normal to the plane, are continuous. Another important fact is these two numbers together with the wavevector fully describe the wave. In the TMM the wave is therefore described as a two-vector. Propagation through a material is then represented by a matrix multiplication, which is for normal incidence given by

$$\begin{pmatrix} E(z+L) \\ F(z+L) \end{pmatrix} = \begin{pmatrix} \cos(k_0 n L) & {}^1/_{nk_0}\sin(k_0 n L) \\ -k_0 n \sin(k_0 n L) & \cos(k_0 n L) \end{pmatrix} \begin{pmatrix} E(z) \\ F(z) \end{pmatrix} \tag{2.9}$$

where $F(z)$ denotes the derivative of $E(z)$ in the z-direction. The implementation of multiple layers is then done by multiplying with a matrix for each layer using the correct (complex) refractive index and thickness for each layer. The reflectivity can then be extracted by reconstructing the field at $z < 0$, which consists of the superposition of the incident wave and the reflected wave. The square of the ratio between these two amplitudes is the reflectivity. As a function of the combined matrix M this is given by

$$R = \left| \frac{(M_{21} + k_{\mathrm{air}}k_{\mathrm{gold}}M_{12}) + i(k_{\mathrm{air}}M_{22} - k_{\mathrm{gold}}M_{11})}{(-M_{21} + k_{\mathrm{air}}k_{\mathrm{gold}}M_{12}) + i(k_{\mathrm{air}}M_{22} + k_{\mathrm{gold}}M_{11})} \right|^2$$

Thus, what we need to know are the refractive indices of both materials. Since fused silica is known to have little non-linearities at these fluences [26], we assume its refractive index remains unchanged at the value of $1.4533 + 1 \times 10^{-7}$ [27] and all the non-linearities happen in the gold. Since the gold absorbs most of the light, the electron temperature will rise as a function of time, making the reflectivity of the gold time-dependent. For each timestep we calculated the reflectivity of the gold, leading to both the absorbance, used to calculated the rise in electron temperature, and the reflectivity. The intensity-averaged value of the reflectivity is taken as the effective reflectivity.

There is however a small problem which makes the application of this method in our situation not exact. The models assumes the light field is in steady-state. Multiple orders of reflections were incident of the material at different times, because the higher the order of reflection, the longer the path travelled through the material. The transfer matrix model assumes however that all reflections experience the same refractive index and thus the same reflectivity. This in practise means the rate of change of the parameters should be slow in comparison to the propagation time through the system. In our system the time for one reflection is approximately 1 fs, only a few order of magnitude shorter then the pulse length. Because of this, it does not improve the simulation to use a time step smaller then this value.

2.3   Refractive index of gold

In order to model the refractive index of the gold, we have used the Drude model. We assume that all the relevant parameters are only a function of, or can at least by be fully described by, the electron temperature. Equation 2.8 then becomes

$$\epsilon_{\text{Au}}(\omega) = \epsilon_{\text{Au,np}} - \left(\frac{\omega_p}{\omega}\right)^2 \frac{1}{1 + \frac{i}{\omega\tau(T)}} \tag{2.10}$$

where,

$$\omega_p = \sqrt{\frac{N Z_{\text{eff}} e^2}{\epsilon_0 m}} \tag{2.11}$$

is the plasma frequency. Z_{eff} indicates the number of free electrons per atom, which is 1 in the linear case, and N is now the *atom* density. The quantity $\epsilon_{\text{Au,np}}$ is the value of the dielectric function of gold in the absence of a electron plasma, which we have taken as 6.0. We then used the values presented by Fourment et al. [28] to couple the temperature to the carrier density. For the relation between the temperature and the Drude damping time, the model presented by Zhang et al. [29] has been used. This model gives the Drude damping time as a function of the carrier density, so we combine it with the above mentioned model for the carrier density. Using the dielectric function, as mentioned in section 2.2, the reflectivity, transmittance and penetration depth are calculated. The penetration depth is combined with the specific

electron heat capacity of gold [30] to calculate the heat capacity, which is used to calculate the change in temperature. A more detailed explanation of the modelling of the refractive index of gold can be found in [31]

2.4   Carrier density of a plasma is water

Since under normal conditions the carrier density in water is negligible, every carrier in water must have been generated by the interaction with the light field. We can describe this with the rate equation

$$\frac{d\rho}{dt} = \left(\frac{d\rho}{dt}\right)_{mp} + \eta_{av}\rho - g\rho - \eta_{rec}\rho^2, \tag{2.12}$$

where the first term describes electron generation by multi-photon absorption, the second term describes electron generation through avalanche ionization, the third describes electron losses through diffusion and the forth describes electron losses due to recombination.

2.4.1   Multi-photon ionization

In these type of simulations, it is typically assumed that water is an amorphous material with a bandgap of $6.5\,\mathrm{eV}$ [32, 33]. Multi-photon ionization is the absorption of k photons, where

$$k = \lceil \frac{E_i}{\hbar\omega} \rceil, \tag{2.13}$$

with ω the frequency of the light and E_i the ionization energy. In our case, for $800\,\mathrm{nm}$ light, $k = 5$. Our common sense dictates us then that the rate must scale with I^5. According to Keldysh theory, which is derived under the assumption that the optical frequency is much larger then the tunnelling frequency, the multi-photon ionization rate is given by [34, 35]

$$\left(\frac{d\rho}{dt}\right)_{mp} = \frac{2\omega}{9\pi}\left(\frac{m'\omega}{\hbar}\right)^{3/2}\left(\frac{Ie^2}{16m'E_i\omega^2 c\epsilon_0 n}\right)^k e^{2k}\Phi\left(\sqrt{2k - \frac{2E_i}{\hbar\omega}}\right) \tag{2.14}$$

with

$$\Phi(x) = e^{-x^2}\int_0^x e^{y^2}dy. \tag{2.15}$$

Here m' is the reduced exciton mass equal to half the electron mass and n the refractive index. Knowing the frequency used, we can, for our experimental conditions reduce this to

$$\left(\frac{d\rho}{dt}\right)_{mp} = 7.3 \times 10^{-4}\omega \left(\frac{m'\omega}{\hbar}\right)^{3/2} \left(\frac{Ie^2}{m'E_i\omega^2 c\epsilon_0 n}\right)^5 . \qquad (2.16)$$

2.4.2 Avalanche ionization

Once a free electron has been generated it can, through inverse bremsstrahlung also absorb energy. If a free electron subsequently collides with a molecule, it can ionize another electron. This will only happen if the kinetic energy of the electron exceeds the ionization energy. At the high photon fluxes we expect, the interaction frequency is dominated by the electron-molecule collision frequency. Under these assumptions, the avalanche ionization rate is given by [35]

$$\eta_{av} = \frac{1}{\omega^2\tau_d^2 + 1}\left(\frac{Ie^2\tau}{mcn\epsilon_0 E_i} - \frac{m\omega^2\tau_d}{M}\right). \qquad (2.17)$$

Here τ_d is the average electron-molecule collision time(and not the same as the Drude damping time in equation 2.8), and is of the order of $1\,\text{fs}$ [35]. M is the mass of the heavy particle, in this case the water molecule. The first term describes the ratio of the acquired energy and the ionization energy. It is thus related to the fraction of electrons ionizing another electron in a collision. Because of momentum conservation, not all energy can be used for ionization. This is incorporated in the second term. When using equation 2.12 it is important to note that it takes time to accelerate and gain enough energy to liberate an electron. This ionization time is roughly equal to k times τ, which is significant for pulses so short. So in order to obtain optimal results, the electron density the avalanche ionization term of equation 2.12 should be evaluated at a time $t - k\tau$

2.4.3 Loss terms

If we compare equation 2.12 with the diffusion equation

$$\frac{\partial \rho}{\partial t} = D\nabla^2 \rho, \tag{2.18}$$

we see that our diffusion parameter g must scale with the square inverse of some typical length scale of the system. This is given by the size of the laser spot. Since a plasma will only be formed where the intensity is high enough, the size of the laser spot will determine the size of the plasma. Parallel to the surface the size will scale with the spot size w_o. Perpendicular to the surface the typical length scale will be the Rayleigh range z_R. A rigorous calculation then gives this equation

$$g = \frac{\tau E_i}{3m}\left(\left(\frac{2.4}{\omega_0}\right)^2 + \left(\frac{1}{z_R}\right)^2\right). \tag{2.19}$$

For the recombination rate, one can use the empirical value of $2 \times 10^{-15}\,\mathrm{m}^3\,\mathrm{s}^{-1}$ obtained by Docchio by measuring the decay of plasma luminescence [36].

2.4.4 Critical density

Using equation 2.8 we can define a critical carrier density N_c for which the Drude term in equation 2.8 becomes significant. Since the value of τ is $10\,\mathrm{fs}$ [37], $\omega\tau$ is of the order of unity and thus we can define the critical density as the carrier density for which the plasma frequency is equal to the optical frequency. This means

$$N_c = \frac{\omega^2 \epsilon_0 m}{e^2} \tag{2.20}$$

which gives a value of $1.7 \times 10^{27}\,\mathrm{m}^{-3}$ for the critical density.
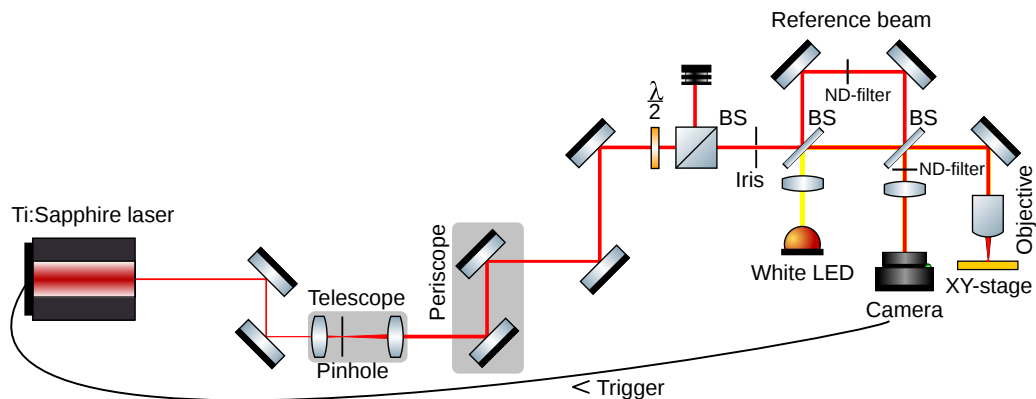
Figure 3.1: A schematic overview of the ablation setup. Image by G. Zomer and M. Scholten

3 Setup

As mentioned in the introduction, the setup was almost build from scratch during this master research. In this section the setup, the modes of operations and the materials used in this research are discussed. In section 3.1 a general overview of the setup is given. Subsequently in Sections 3.2 up to and including 3.3 the individual parts are explained and described more elaborately. Section 3.4 deals with the specific settings and actions used in the experiments performed. Finally, Section 3.5 describes the properties of the samples used in the experiments.

3.1 General overview

A general overview of the setup can be seen in Figure 3.1. In the left of the picture a Ti:Sapphire laser is depicted. It produces an 800 nm laser pulse. This pulse is led through a telescope. The telescope consists of a pair of lenses with focal lengths of 50 mm and 125 mm respectively. This combination creates a magnification of 2.5, with a lens separation of 211 mm. The discrepancy between this number and the sum of the focal lengths is partly because the beam leaves the laser slightly divergent and partly to establish a weak focus at the position of the back focal plane of the objective. In the glass on gold measurement, a pinhole with a diameter of 300 μm was places in the common focus in order to spatially filter the beam. Due to energy constraints, this was not possible for the measurements on water.

Then the beam gets elevated in the vertical direction by a periscope. On the first level the beam passes a $\lambda/2$ plate, directly followed by a polarizing beam splitter(PBS) cube. A waveplate mirrors the polarization with respect to its principle axis. Thus by rotating the waveplate it is possible to give the beam an arbitrary polarization,

Figure 3.2: A camera image. On the right it shows the reference beam. On the left the focus can be seen.

thus controlling the amount of light reflected and transmitted by the PBS. The $\lambda/2$ plate is mounted on a computer controlled motorized rotational stage [T-RS60A, Zaber Technologies Inc.]. This gives us the ability to change the pulse energy fast and automatically during the experiment. With this we can achieve a contrast ratio of approximately 3000.

Next the beam passes an iris, with a diameter roughly equal to the diameter of the beam. This is necessary because the beam profile has an aspect ratio of approximately 3 at this position, leading otherwise to a distorted and elliptical beam profile at the sample. Since the measurements on silica on gold used a spatially filtered beam at this point, the iris was not used for these measurements.

Subsequently the beam passes a pellicle beam splitter (Thorlabs BP108), where 93,9% of the light gets transmitted, and 6,1% gets reflected into the line labelled *Reference beam*. This line also contains an ND-filter. Both beams are led to a second pellicle beam splitter of the same type. For the measurements on water, the first beam splitter was absent. There the second beamsplitter provided the reference beam, which then passed the ND-filters, reflected back of a mirror, passed the ND-filter again and arrived back at the second beam splitter. This is not shown in the figure.

The reference beam gets transmitted towards the camera, while the main beam gets transmitted towards the sample. It is then deflected downward to the NA = 0.8 infinity corrected objective (NIKON MUE20901), which focusses it on the sample. The objective has a magnification of 100x, with an effective focus length of 2 mm and a working distance of 3.5 mm. It is mounted on a computer controlled motor stage (T-LSM025A, Zaber Technologies Inc.) which allows us to move the objective in the z-direction with a resolution of 48 nm. The solid samples are placed on a two axis motorized computer controlled stage (M-686.D64, Physik Instumente), giving a sub-micrometer control over the lateral position of the sample.

In order to retrieve visual information about the sample, a white light illumination setup has been build. It consist of an LED and a 100 mm lens placed at a distance of
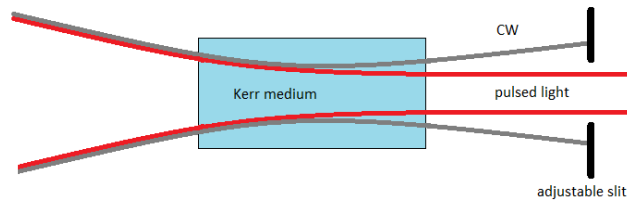
Figure 3.3: Kerr lensing schematically. Image by M. Bruinewoud [38]

142 mm. This slightly convergent beam is then coupled into the beam path by the first beam splitter. On the sample this gives a field of view of approximately 50 μm. The LED is switched off during data acquisition.

The light coming back from the sample is (partially) reflected by the second beam splitter. It then passes a 200 mm lens which is mounted at a distance of 200 mm from the camera(Andor Zyla 5.5). A trigger line is connected from the camera to the laser, via an microcontroller [Arduino] and a delay box [DG535, Stanford Research Systems]. The microcontroller is connected to the computer and can be used to block the trigger signal coming from the camera. The box is set to a delay of 5 ps. This has no function in the setup other then to drive the input impedance of the laser controller.

3.2 Laser theory and operation

The laser used in this research was a Coherent Mira 900 in combination with an APE pulseSwitch cavity dumper. The gain medium is a Titanium:sapphire crystal pumped externally by a 4.5 W laser beam at 532 nm from a Coherent Verdi. Modelocking is achieved by Kerr lensing. Because a laser pulse has a higher intensity then the continuous wave (CW) mode, due to the Kerr effect it experiences a different refractive index. Thus it is established that the pules mode has a smaller waist then the CW mode. This is illustrated in figure 3.3.

When a slit with adjustable width is then placed in the beampath, it is possible to interrupt the edges of the CW mode, while leaving the pulsed mode mostly unaffected. By choosing an appropriate width, the gain coefficient of the CW mode becomes smaller then 1, while keeping the gain coefficient of the pulsed beam above 1.

However this method will only enforce an already existing pulse. The random fluctuations created during CW operation are not strong enough to create sufficient Kerr lensing. As a starting mechanism the cavity length is modulated at the proper speed, inducing very high power fluctuations. Once modelocking is reached, the length modulation is stopped. In this system the cavity length is modulated by tipping the angle of a glass plate, thus changing the amount of distance travelled in a high index medium, effectively changing the cavity length. The combination of these techniques
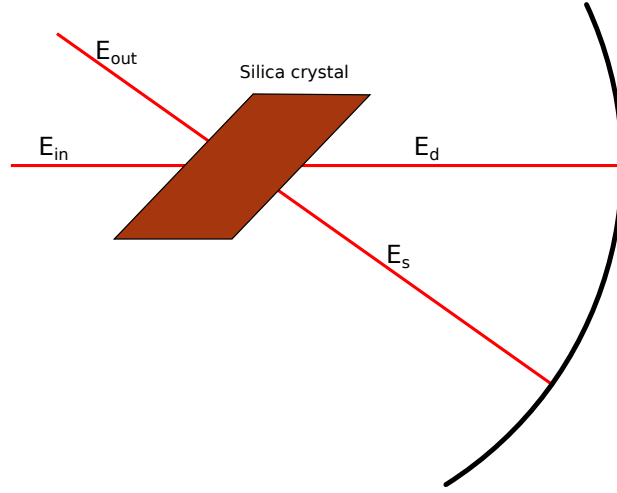
11

Figure 3.4: Schematic image of the double-pass Cavity Dumping. Image reproduced by the author after [40].

creates pulses of 165 fs [39].

A single laser pulse produced in that way has a very low energy as well a very high repetition rate of 54 MHz. It is possible to use a pulse picker, acting outside the laser cavity, but this would reduce the pulse energy further. It is better to select the pulses inside the cavity, so the pulses which are not selected can add to the intra-cavity power. Instead of a high reflector and an output coupler, the cavity now contains two high reflectors thereby increasing the intra cavity power [40]. In order to couple the desired pulses out double pass cavity dumping is used. For this a fused silica crystal is inserted into the beampath. Once a pulse needs to be selected a high frequency acoustic signal(HFAS) is applied to the crystal. Due to the acousto-optical effect the density and consequently the refractive index of the crystal changes. This refracts the beam towards a mirror which reflects it back to the crystal(see figure 3.4), where is passes a second time.

Lets assume the incoming pulse can be described by:

$$E_{in} = E_0 \cos(\omega t), \tag{3.1}$$

where E is the electric field and ω the frequency. Due to the phonon-photon coupling the light will pick up an increase in frequency equal to the HFAS frequency, Ω. There will also be a phase difference between the incoming pulse and the HFAS, we will denote this as ϕ. Given a diffraction efficiency η this gives the following expression for the field of the diffracted pulse:

$$E_{s} = \sqrt{\eta}E_0 \cos(\omega t + \Omega t + \phi), \tag{3.2}$$

and the depleted pulse

$$E_d = \sqrt{1 - \eta} E_0 \cos(\omega t + \Omega t + \phi) \tag{3.3}$$

During the second pass the beams couple again so the output beam is the sum of the unperturbed diffracted beam and the diffracted depleted beam.

$$E_{out} = \sqrt{\eta(1 - \eta)} E_0 (\cos(\omega t + \Omega t + \phi) + \cos(\omega t - \Omega t - \phi)). \tag{3.4}$$

Squaring this gives for the output intensity I_{out}

$$I_{out} = 4\eta(1 - \eta) I_0 \cos^2(\Omega t + \phi). \tag{3.5}$$

In practise this system works not as perfectly as suggested above. Also when no HFAS is applied to the crystal, part of the beam gets coupled out of the cavity. The energy of these pulses is low, approximately 50000 times lower then a selected pulse, but due to their high repetition rate they form a significant part of the background.

3.3 Camera system

As mentioned the camera is an Andor Zyla 5.5. It has a CMOS (Complementary Metal Oxide Semiconductor) image sensor of 2560 by 2160 pixels. The size of each pixel is 6.5 μm, which together with the 100x magnification of the objective gives an effective pixel size of 65 nm. The main difference with a CCD sensor is that a CMOS has a readout structure for each pixel separately, which also means different pixels have different readout noises. One of the benefits of CMOS is that the readout noise is much lower then that of a CCD, 1 or 2 electrons compared to 6 to 10 [41].

All pixels are exposed and read out simultaneously. This puts a lower limit to the exposure time of 9.34 μs per row. In order to lower the exposure time, an explicit region of interest is chosen. The region is chosen such that it is as small as possible, while both beams are fully captured. By positioning the region of interest in the center of the camera another reduction of a factor of two in the exposure time is obtained. A region of interest of 200 by 130 pixels was chosen for the water measurements, with an exposure time of 650 μs. For the solid state measurement, since the beam was spatially filtered better, a region of interest of 170 by 60 pixels sufficed, with an exposure time of 300 μs. A trigger output is then generated for the duration of the exposure, which is then send to the laser.
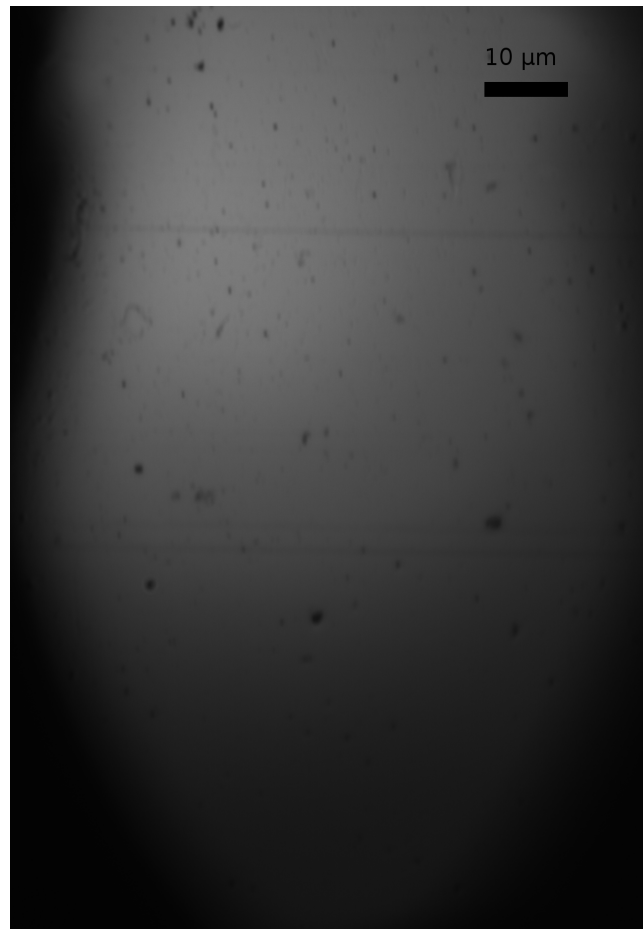
Figure 3.5: An average section of the sample. This part can not be used for measurements, since the chances of hitting a dustpiece or hole is too large. This image is taken using the white light illumination mode of our setup.

3.4   Mode of operation

A measurement starts with the visual identification of a clean part of the sample. Since most of the sample is covered in holes and dust(see Figure 3.5), this is a non-trivial task. This also prevents us from taken subsequent measurements close to the original ones. A detailed description of the positions of measurements is shown in appendix A.

Subsequently the objective position is modified to optimize the spot size. This is done by the human operator by inspecting the signal from the background pulses. The size, the peak intensity as well as the absence of fringes are used to judge the position of the focus. This can be done for solids with an accuracy of $150\,\mathrm{nm}$, well within the depth of focus. Due to large vibrations of the water surface this accuracy is not reached for water. Here the accuracy is limited to approximately $500\,\mathrm{nm}$. The fluences used
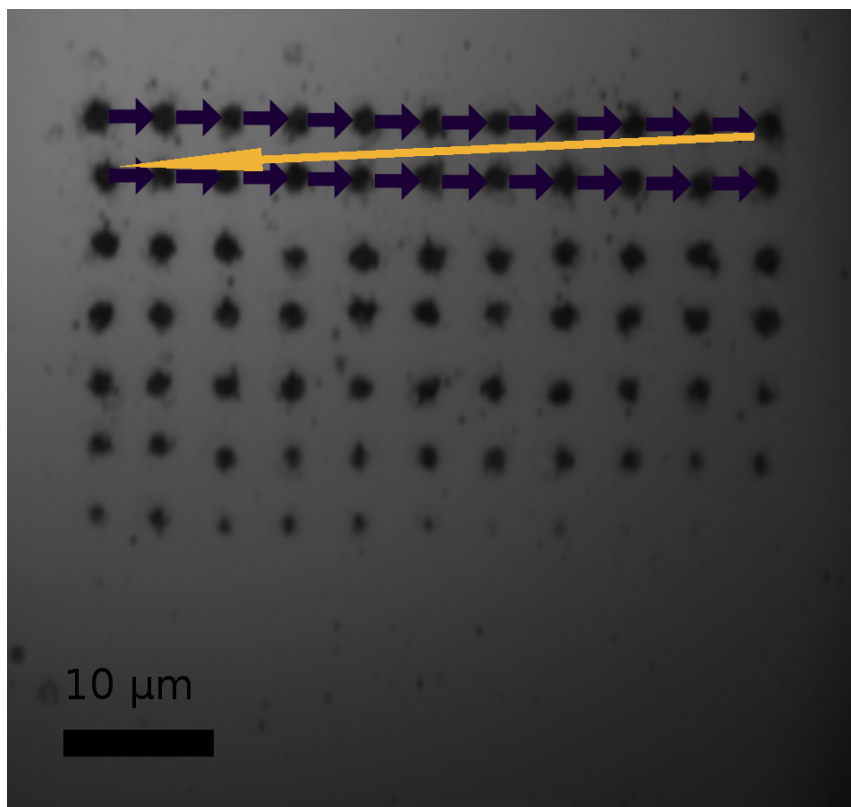
14

Figure 3.6: A typical field after measurements in the white light illumination mode. The arrows indicate the sequence of measuring. Note that in reality the laser does not move, the sample moves instead

during this procedure are low enough to ensure that, even for a repetition rate of 54 MHz, no damage is inflicted.

One measurement consist of a field of multiple shots. Before each shot, first a background frame is shot at the same position. For this purpose the trigger line in blocked. Subsequently one shot is let through by opening the trigger line. After this the sample is moved. This is done is steps of 5 μm in a typewriter array (see figure 3.6). This distance is chosen so the debris of a crater will not interfere with the next shot. The total number of shots in a field is limited by the average size of a clean area on the sample. The number of shots per field was either 100 or 121. The tilt of the sample has been compensated and is smaller then 1:300. This means the focussing error at the lower rightmost shot is not larger then 300 nm, within the depth of focus.

For water the movement of the sample is not necessary and even counterproductive. Since in the ablation of liquids not permanent damage is done, the shot position is afterwards undistinguishable from the other parts of the surface. Moving the sample on the other hand would induce vibrations in the water which would worsen the focus.

3.5   Material samples

The water used is ultrapure water with a resistivity of $18\,M\Omega\,cm$. During measurements the water was in a standard aluminium weighing dish. Before use the dish was cleaned by sonicating the dish for half an hour while filled with pure water. Both the dishes and the water were kindly provided by the group of Alfons van Blaaderen.

The silica on gold samples were made of a thick layer of silicon for bulk. This is covered with a thin layer of gold, though thick enough to be able to ignore reflection on the silica-gold interface. The gold was then coated with layers of silica. In total six different thicknesses were produced $65\,nm$, $85\,nm$, $115\,nm$, $145\,nm$, $165\,nm$ and $185\,nm$. Of these samples, the thicknesses of $85\,nm$ and $185\,nm$ was not used due to practical limitations. For technical reasons, the sample contains also patches without silica. Measurement on these regions were also performed. A more elaborate discussion of the production process is discussed in [23]. We thank Paul Planken for donating the samples.

4 Results

4.1 Water

For each shot the camera captures two beams. One is the reference beam, which has not passed the objective or the sample and is thus a measure of the incident energy. The other is the reflected beam, which contains the reflected light, coming back from the sample. Hence the picture which is captured for each shot is split in two. The right part originates from the reference beam. To calculate the energy the ADC-values are summed and then the sum of the ADC-values of the background picture is subtracted. This is also done for the left part, which is the reflected light. The ratio of these two numbers is the reflectivity.

Further the Gaussian function of equation 4.1 is fitted to the picture.

$$I(x,y) = I_0 e^{-2\left(\frac{(x-x_0)\cos(\theta)+(y-y_0)\sin(\theta)}{\omega_{0,x}} + \frac{(x-x_0)\cos(\theta)-(y-y_0)\sin(\theta)}{\omega_{0,y}}\right)} \tag{4.1}$$

This function describes a 2D Gaussian centered around $\left(\begin{smallmatrix} x_0 \\ y_0 \end{smallmatrix}\right)$ with unequal widths in the major axis direction and minor axis direction of $\omega_{0,x}$ and $\omega_{0,y}$ respectively. The major axis is rotated with an angle θ with respect to the x-axis. Given a beam with these properties the average fluence F_{av} is defined as

$$F_{av} = \frac{P}{\pi \omega_{0,x} \omega_{0,y}} = \frac{I_0}{2}. \tag{4.2}$$

Calibration

These value of the fluence and the reflectivity are relative values however. We therefore need to calibrate the camera signal to a known energy. The average power at our operation repetition rate of $1\,\mathrm{Hz}$ is to low to be accurately measured. For our calibration we used a higher repetition rate. For low repetition rates, such as the ones used in this research the pulse power is independent of repetition rate [40]. A repetition rate of $1.538\,\mathrm{kHz}$ was used with a camera exposure time of $650\,\mathrm{\mu s}$. In this way the exposure time was the same as in the experiment, while at the same time receive a single pulse. That last condition is necessary, since we can no longer trigger the setup with the camera as it is not fast enough to generate a kHz-trigger signal.

The power at the sample was measured by replacing the sample with a Coherent Fieldmate powermeter. Naturally for each power, a background shot was taken, for which also the power was taken. The powers were varied by rotating the waveplate as described in section 3.1. The background due to external light on the powermeter was measured to be less then 10% of the lowest measured power.
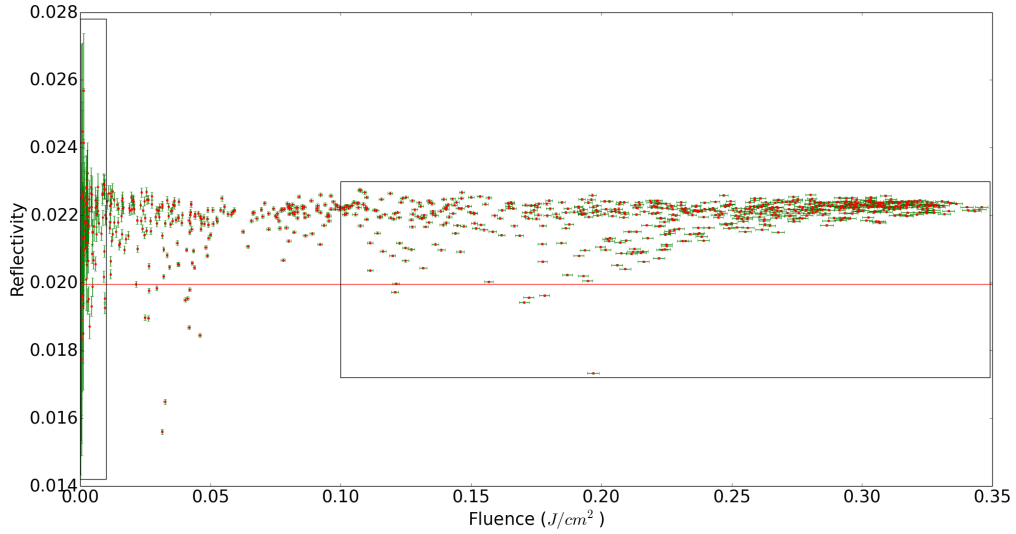
17

Figure 4.1: Measurements of the reflectivity as a function of fluence. The red line denotes the linear value of the reflectivity. The black boxes denote the plotted areas of figure 4.2 and 4.3

In order to calibrate the reflectivity we need to measure the reflectivity of a sample of known reflectivity. To do this, we assumed the reflectivity is not altered for low fluences, and is thus equal to the Fresnel-value of $0.019\,955$ [42]. While we have some measurements of the reflectivity for low fluences, they experience a lot of shot noise. Furthermore, as we will show in the subsequent parts of this paragraph, already for very low fluences we see a rise in reflectivity.

We thus employ a trick. The background shots, especially at high fluences, consist mostly of unpicked pulses, as discussed in section 3.2. These pulses individually have fluences which are 10 times lower then even the lowest fluence used in the experiment. However since about $35\,000$ pulses get captured within one exposure time, the relative shot noise is comparable to the highest fluences, which is well below 1%. The low-fluence background shot have hardly any contribution from the background pulses and contain mostly 'normal' background. We use these shots to subtract the normal background from the high-fluence background shot so that only the background pulses remain. The reflectivity was then linearly scaled so that this reflectivity is equal to $0.019\,955$.

The results of the measurements and these calibration can be seen in figure 4.1. As can be seen on the high fluence side, the values are reasonably consistent and differ significantly from the linear value. This can be seen even more clear if we zoom in on the right part of the graph, showed in figure 4.2. The most interesting behaviour can be seen in figure 4.3, which has been zoomed-in on the ultra-low fluence regime. We see that the uncertainty becomes larger, since $\Delta R \propto 1/\sqrt{N} \propto 1/\sqrt{F}$. But
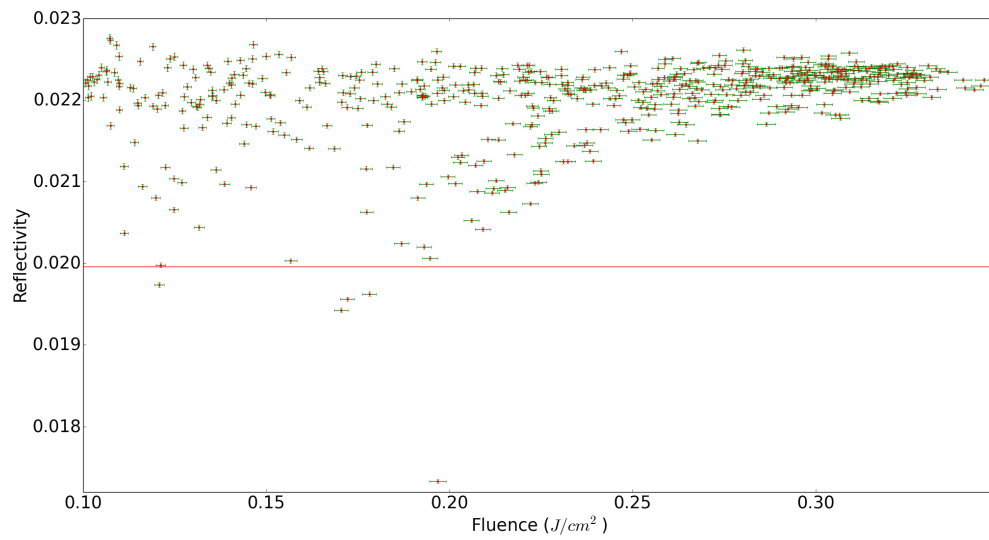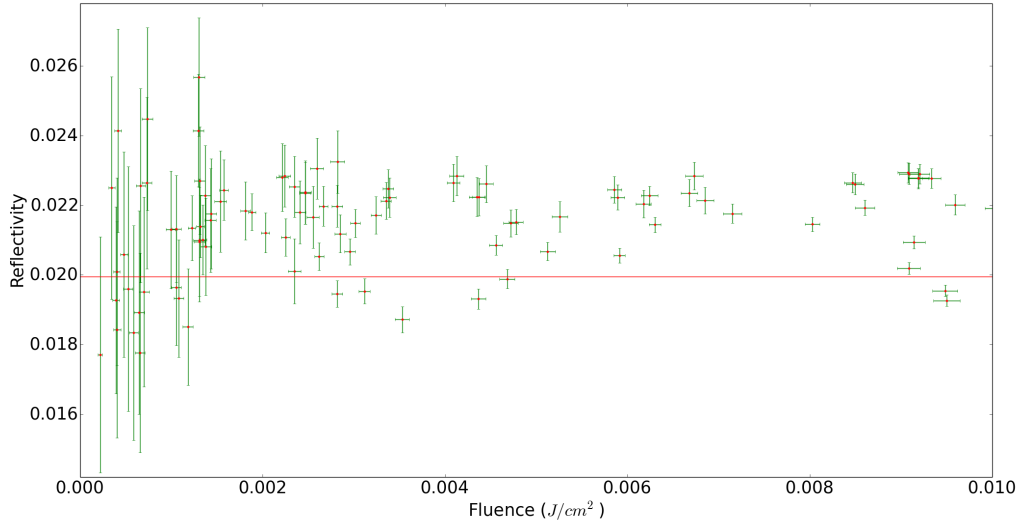
Figure 4.2: Measurements of the reflectivity as a function of fluence. The red line denotes the linear value of the reflectivity. Zoomed-in version of the high-fluence part.

most importantly there is a drop in reflectivity for fluences lower then approximately $1\,\mathrm{mJ\,cm^{-2}}$. Collectively these point differ significantly from the high-fluence limit of 0.0223, while agreeing with the linear value of 0.019 955.

We can also observe that the rise in reflectivity is very fast. Already at fluences of $2\,\mathrm{mJ\,cm^{-2}}$, the reflectivity differs hardly from 0.0223.

Figure 4.3: Measurements of the reflectivity as a function of fluence. The red line denotes the linear value of the reflectivity. Zoomed-in version of the low-fluence part.

4.2 Silica on Gold

4.2.1 Simulations

If we simulate the reflectivity of a thin layer of silica on a thick layer of gold, as discussed in sections 2.2 and 2.3, using the layer thicknesses of section 3.5, we produce the graphs of figure 4.4.

First of all, we can see that already at low fluences, the presence of the silica layer lowers the reflectivity. This is because the refractive index contrast between gold and silica is lower then that between gold and air. The silica-air interface does not reflect enough to compensate for that.

Besides we see a decrease of the reflectivity of the gold for increasing fluence, corresponding with both theory and the input model. We also see this decrease, albeit stronger, in the simulations with added silica.

Furthermore we see the effect of the interference. First the reflectivity goes down for increasing silica layer thickness, until the thickness reaches $115\,\mathrm{nm}$, after which the reflectivity goes back up again. This minimum is approximately equal to $\frac{\lambda_{vac}}{4n} = 138\,\mathrm{nm}$, which indicates destructive interference between successive reflections. The deviation comes from the non-zero phase jump at the silica-gold interface. The last thing to note is that for samples with a lower reflectivity the drop in reflectivity happens at a lower fluence.
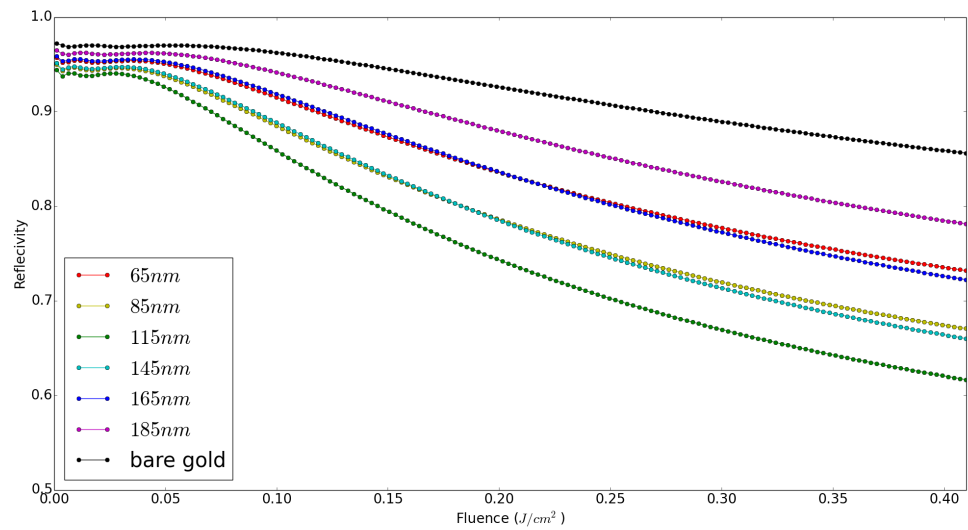
Figure 4.4: Simulation of the reflectivity of gold with layers of different thickness of silica on top. Different colors indicate different thicknesses.
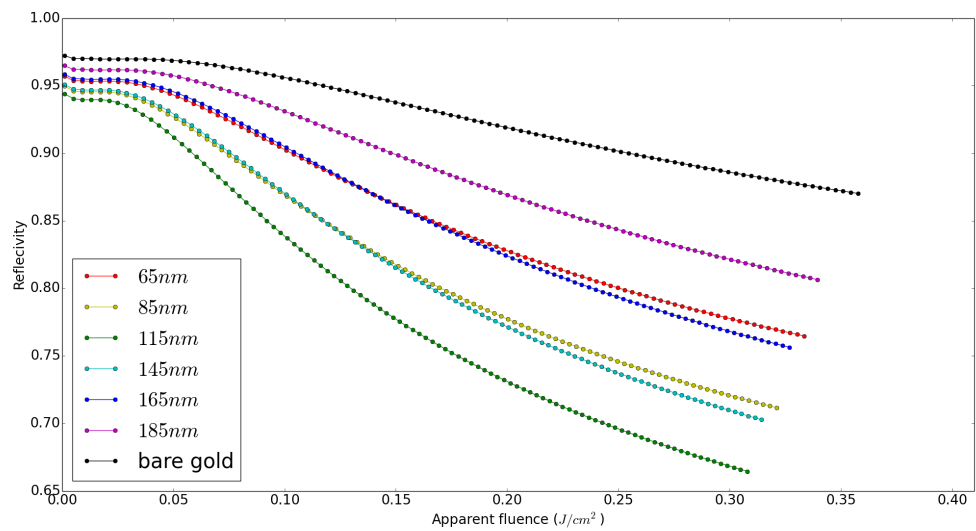

Figure 4.5: Simulation of the reflectivity of a Gaussian beam on a gold with layers of silica of different thickness as a function of the apparent average fluence.

A Gaussian beam has of course a higher fluence in the center then at the edges. Since a higher fluence means lower reflectivity, the edges get amplified relative to the center upon reflection. This results in a broader reflected beam. Since we will again attempt to use the algorithm described in section 4.1, more specifically equation 4.1, to determine the incident fluence, we will overestimate the incident spotsize and therefore underestimate the incident fluence. We also modelled the effect of this. Since the diffusion takes place on a long timescale compared to the pulse [35], we can assume each infinitesimal surface element to reflect the same percentage of the incident light as a plane wave with the same fluence as the local fluence would.

We can use this to define an apparent fluence. This is the energy of the incident beam, divided by the spot size of the reflected beam. This is namely what is actually measured by the system, following the algorithm of section 4.1. This correction changes figure 4.4 into figure 4.5. First of all, the graphs no longer stop at $0.4\,\mathrm{J\,cm^{-2}}$, because of the pulse broadening. For the highest fluences this effect increases the spotsize by approxmimately 15%, hence the lines now top around $0.35\,\mathrm{J\,cm^{-2}}$. This broadening is different for each thickness, and therefore the line stops at different fluences for different thicknesses.

Finally the reflectivity is higher for high fluences. This is logical since a pulse with a certain fluence is not a plane wave with that fluence. It contains regions with a higher then average fluence, and areas with a lower then average fluence. The first ones lower the total reflectivity, while the second ones increase the total reflectivity. But as can be seen in figure 4.4 for high fluences the graphs evens out. This means the increase of the reflectivity will be the dominant effect.

4.2.2 Measurements

In total 24 fields were shot, composed of 121 shots each. This was done on two subsequent days. On each day, for each section of the sample, two field were shot. Usually the time difference between two fields on the same section was in the order of minutes. The details of the fields are discussed in Table 4.1. The relative location of each field is shown in the appendix.

After each all fields were shot, the sample was investigated using white light illumination. For each shot we determined whether ablation occurred or not. For some shots the ablation crater was very small, almost negligible. These were classified as a separate category.

Field	Section	Thickness	Figure	Day	Marker style
51	6	Bare gold	4.6	1	square
52	6	Bare gold	4.6	1	diamond
73	6	Bare gold	4.6	2	circle
74	6	Bare gold	4.6	2	triangle
53	4	Bare gold	4.7	1	square
54	4	Bare gold	4.7	1	diamond
68	4	Bare gold	4.7	2	circle
69	4	Bare gold	4.7	2	triangle
48	5	65 µm	4.8	1	square
49	5	65 µm	4.8	1	diamond
71	5	65 µm	4.8	2	circle
72	5	65 µm	4.8	2	triangle
55	1	115 µm	4.9	1	square
56	1	115 µm	4.9	1	diamond
66	1	115 µm	4.9	2	circle
67	1	115 µm	4.9	2	triangle
57	2	145 µm	4.10	1	square
58	2	145 µm	4.10	1	diamond
64	2	145 µm	4.10	2	circle
65	2	145 µm	4.10	2	triangle
59	3	165 µm	4.11	1	square
60	3	165 µm	4.11	1	diamond
62	3	165 µm	4.11	2	circle
63	3	165 µm	4.11	2	triangle

Table 4.1: Overview of the different measurement field. Field- and sectionnumber match the numbers in the appendix. Marker style refers to the Figures 4.6 up to and including 4.11

Calibration

For technical reasons and reasons discussed further in this paragraph no separate calibration was performed. Instead the calibration discussed in Section 4.1 was reused. In between some filters in the setup were switched. This has been corrected by inserting their fabrication transmission at the correct wavelength. The reflectivity was calibrated using the simulation results at low fluence. This was chosen since calibration using unpicked pulses led to erratic results.

Using this procedure meant that the data from day 1 significantly differed from the data of day 2. Within one day, measurement from two different field were indistinguishable. We scaled fluence for both days such that the ablation threshold for both datasets overlapped. The difference in scaling needed is in the order of a few percent. In that case the datasets of both days become indistinguishable as well. This leads us to believe that the calibration apparently varies over time. We therefore can not guarantee the absolute value of all fluences, but we can guarantee the relative values.
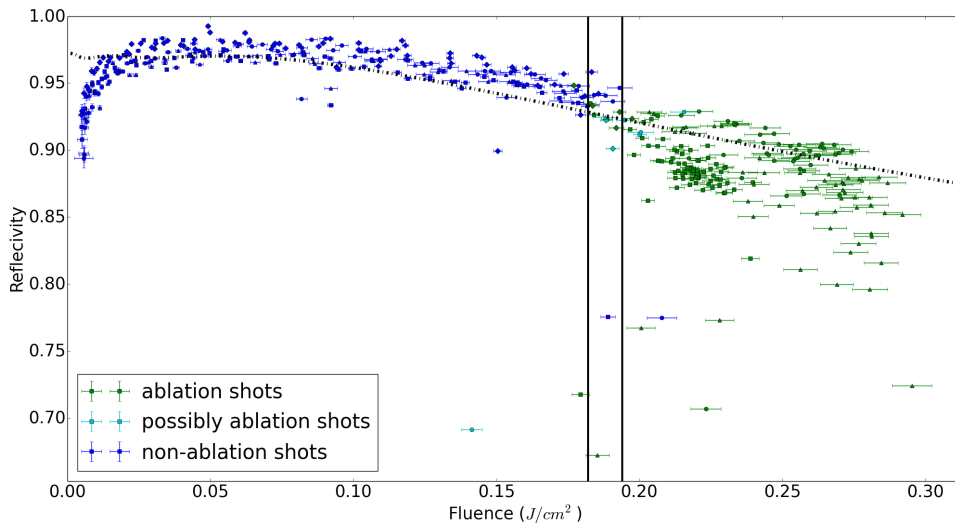

Figure 4.6: Reflectivity as a function of incident fluence for a sample of gold(Section 6). A blue marker indicates a shot after which no damage was observed. A green marker indicates a shot with observed damage. A cyan marker indicates indicates negligible, but still observable damage. The vertical lines represents were, based on these observation, the domain in where the ablation threshold lies. Four different fields were created for this graph, they are indicated with different marker style according to Table 4.1. The dashed line is the corresponding line form Figure 4.5.
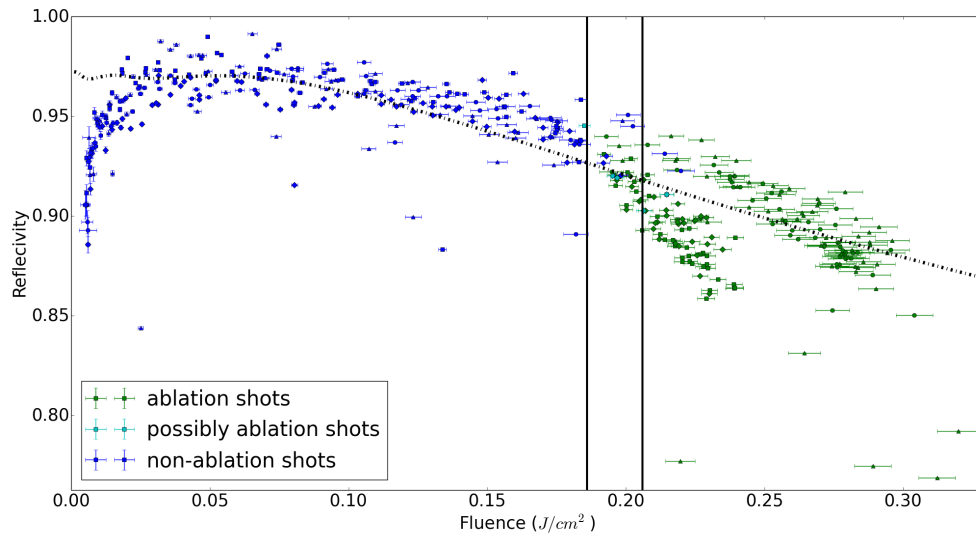
Figure 4.7: Reflectivity as a function of incident fluence for a sample of gold(Section 4). A blue marker indicates a shot after which no damage was observed. A green marker indicates a shot with observed damage. A cyan marker indicates indicates negligible, but still observable damage. The vertical lines represents were, based on these observation, the domain in where the ablation threshold lies. Four different fields were created for this graph, they are indicated with different marker style according to Table 4.1. The dashed line is the corresponding line form Figure 4.5.

The results can be found in Figures 4.6 up to and including 4.11. In each graph, just as in Section 4.1, the reflectivity is plotted as function of fluence. The different categories of ablation damage is denoted with color. A green marker indicates significant observed damage. A blue marker indicates no observed damage. A cyan marker indicates negligible, barely observable damage. This allows us to set an upper and lower limit for the ablation threshold. These are indicated by the vertical lines in the figures. The lower limit is chosen as the lowest fluence for which ablation is observed, barring statistical outliers. The upper limit is the lowest fluence for which we consistently see ablation. Note that there are still measurements at a higher fluence, which do not show traces of ablation.

Each figure contains the data of four different fields. They are shown by their different marker styles. For each figure the first field of the first day has a square marker. The second field of the first day has a diamond marker. The first field of the second day has a circular marker, and the second field has a triangular marker.
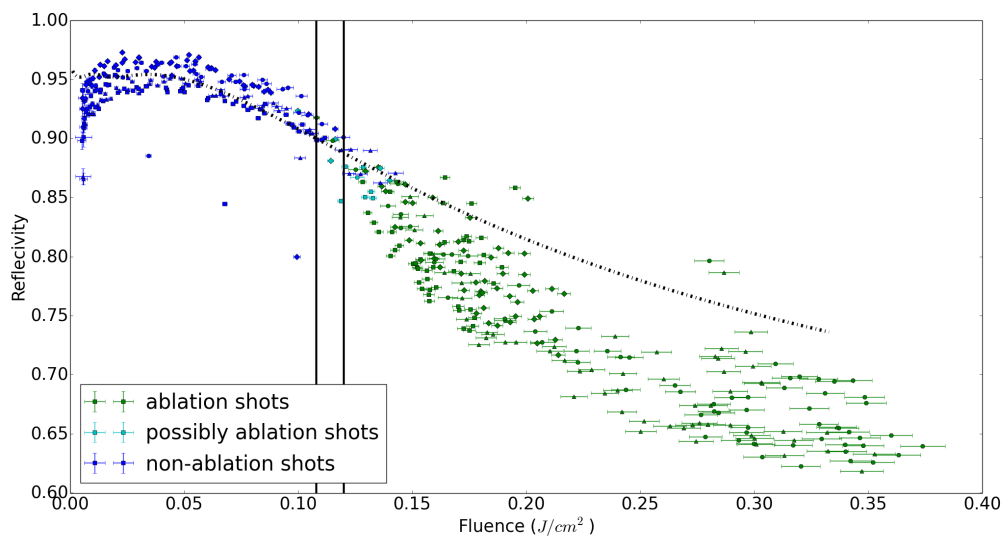
25

Figure 4.8: Reflectivity as a function of incident fluence for a sample of gold with a silica layer of $65\,\mathrm{nm}$ on top. A blue marker indicates a shot after which no damage was observed. A green marker indicates a shot with observed damage. A cyan marker indicates indicates negligible, but still observable damage. The vertical lines represents were, based on these observation, the domain in where the ablation threshold lies. Four different fields were created for this graph, they are indicated with different marker style according to Table 4.1. The dashed line is the corresponding line form Figure 4.5.
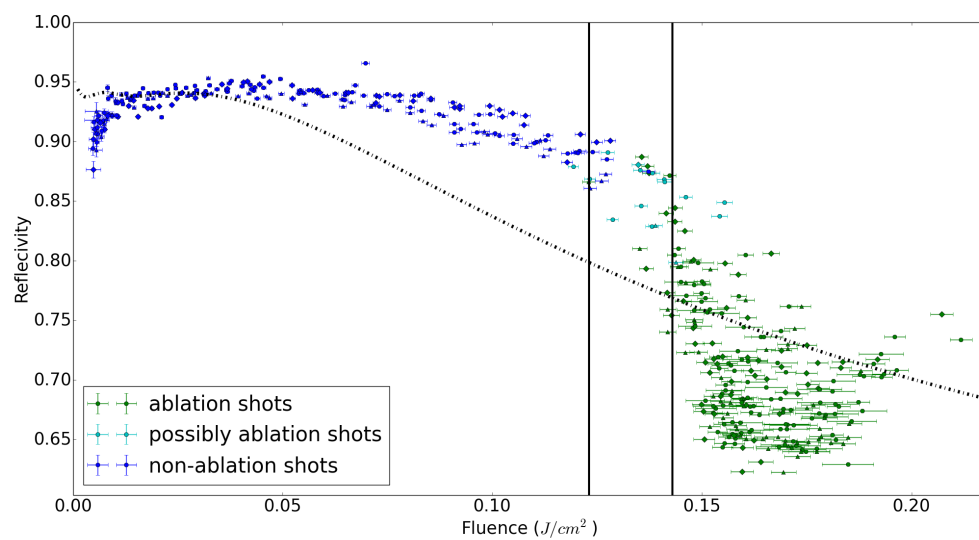
Figure 4.9: Reflectivity as a function of incident fluence for a sample of gold with a silica layer of $115\,\mathrm{nm}$ on top. A blue marker indicates a shot after which no damage was observed. A green marker indicates a shot with observed damage. A cyan marker indicates indicates negligible, but still observable damage. The vertical lines represents were, based on these observation, the domain in where the ablation threshold lies. Four different fields were created for this graph, they are indicated with different marker style according to Table 4.1. The dashed line is the corresponding line form Figure 4.5.
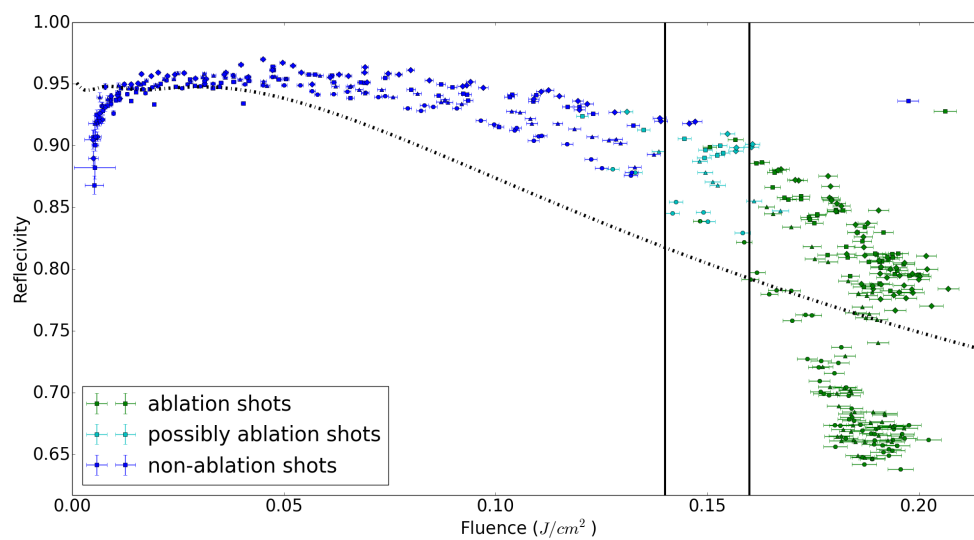
Figure 4.10: Reflectivity as a function of incident fluence for a sample of gold with a silica layer of $145\,\mathrm{nm}$ on top. A blue marker indicates a shot after which no damage was observed. A green marker indicates a shot with observed damage. A cyan marker indicates indicates negligible, but still observable damage. The vertical lines represents were, based on these observation, the domain in where the ablation threshold lies. Four different fields were created for this graph, they are indicated with different marker style according to Table 4.1. The dashed line is the corresponding line form Figure 4.5.
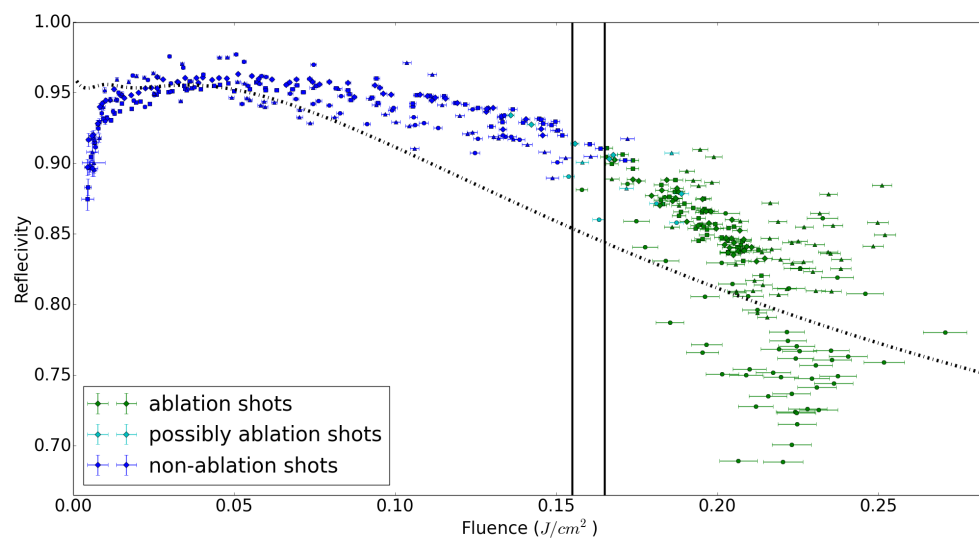
Figure 4.11: Reflectivity as a function of incident fluence for a sample of gold with a silica layer of $165\,\mathrm{nm}$ on top. A blue marker indicates a shot after which no damage was observed. A green marker indicates a shot with observed damage. A cyan marker indicates indicates negligible, but still observable damage. The vertical lines represents were, based on these observation, the domain in where the ablation threshold lies. Four different fields were created for this graph, they are indicated with different marker style according to Table 4.1. The dashed line is the corresponding line form Figure 4.5.

We can see in Figures 4.6 and 4.7 that the reflectivity of a sample of bare gold starts of constant, after which it slowly but constantly drops, as a function of fluence. We also see a steep rise in reflectivity for the lowest fluences. We see that also in the Figures 4.8 to 4.11. Whether this rise is physical, or that there is a constant background, only in our measurement of the incident fluence(despite our background subtraction) can not be determined from the data due to the low signal to noise ratio for low fluence. Apart from this we see that the data agrees very well with the simulation.

When we look at Figure 4.8, we see the reflectivity of the sample with a silica layer of 65 nm. We observe qualitatively similar behaviour compared to Figures 4.6 and 4.7. The drop in reflectivity is however much more pronounced. We see that the measurements agree qualitatively with the simulations, but it only agrees qualitatively for low fluence. For high fluence, the simulation significantly overestimates the reflectivity.

In Figures 4.9 and 4.10 the reflectivity for the samples with thicknesses of 115 nm and 145 nm are shown. We see that the simulations also no longer describe the data qualitatively. We see the reflectivity remain constant over, compared to the previous samples, a broad range of fluences. After a certain threshold is passes, which coincidently lies around the ablation threshold, the reflectivity drops very suddenly as a function of fluence. Note that this reflection threshold lies at a higher fluence for 145 nm then for 115 nm.

Figure 4.11 shows the same for a thickness of 165 nm. We see qualitatively the same behaviour as in the previous two figures. The drop in reflectivity is however less pronounced at at even higher fluence.

4.2.3 Discussion

In order to account for the sudden drop in reflectivity we have come up with a model. In Section 2.2 we assumed that the refractive index of the silica will not change significantly under the influence of the incident light field. This does not happen because the absorbance of the silica is too low. Hence there will only be a small rise in electron temperature. In this system it is however not strictly necessary that the silica absorbs the energy. It is in principle possible for the gold to absorb the energy and then transfer it to the silica.

Thermal conduction is much to slow to accommodate this, since during the pulse the thermal energy of the gold is solely in the electrons, and not yet in the lattice. The only mechanism fast enough is is the penetration of fast electrons from the gold into the silica. There will of course be an energy barrier since the Fermi level will differ in both materials.
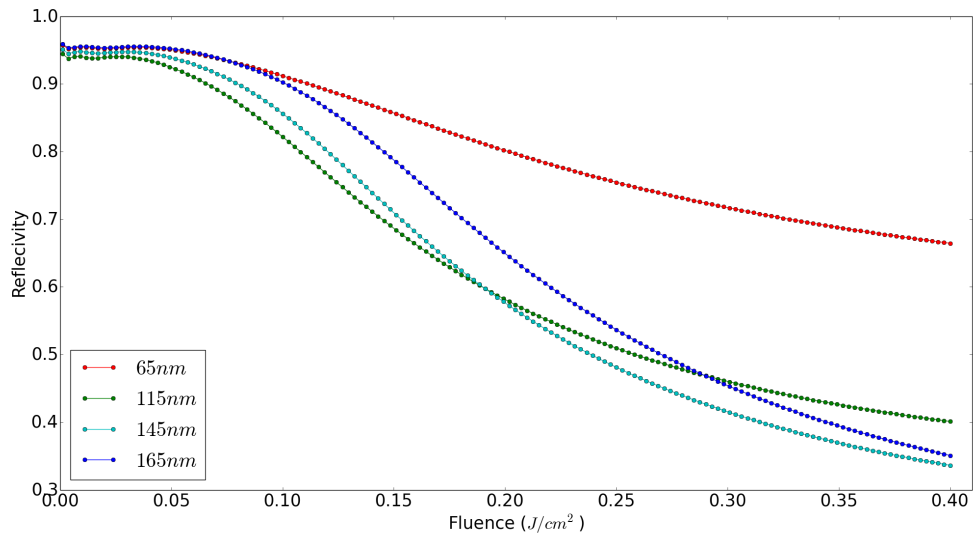
Figure 4.12: Results of the simulation of the reflectivity of gold with layers of different thickness of silica on top. Penetration of hot electrons into the silica has been taken into account.

We modelled this by adding the possibility of carriers in the silica to the model of Section 2.2. We did that by adding a Drude term to the dielectric function of silica. The carrier density n_{Si} is taken to be equal to the carrier density in the gold n_{Au}, but then scaled with a Boltzmann factor

$$n_{Si} = n_{Au} e^{\frac{\Delta E}{k_b T}}.$$ (4.3)

If we add this to the model we end up with Figure 4.12.

In this figure we can see a number of interesting features. First of all we must conclude that the drop is not as steep as we see in the data. The reflectivity is however much lower then in the previous simulation (Figure 4.4). This is probably mostly due to absorption in the silica layer. We can see that the lowering of the reflectivity is much bigger for thicker layers of silica. The layer of 65 nm only has a small effect, just as we see in our experimental data. The effect only grows significance at thicknesses larger then 115 nm. We also see that the drop in reflectivity happens at higher fluence for higher thickness. The last indication is that this graph is produced for $\Delta E = 5\,\text{eV}$. This value has the right order of magnitude for these kind of energy differences. We can not compare this to theory, since this depends very strongly on the exact crystal structure of the silica.
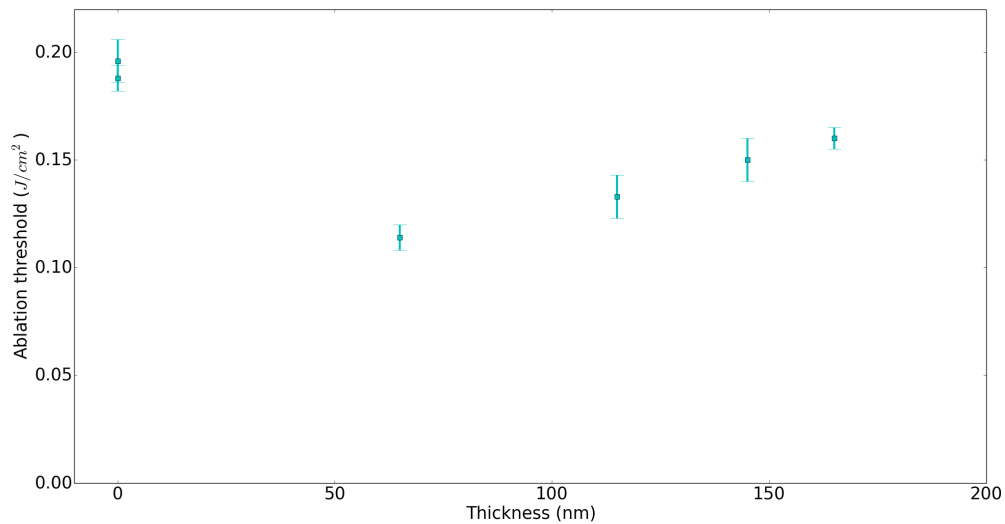
31

Figure 4.13: Ablation threshold as a function of thickness of the silica layer.

4.2.4 Ablation Threshold

If we read off the ablation threshold from Figures 4.6 up to and including 4.11, we get Figure 4.13. It can clearly be seen that the ablation threshold is the highest for a sample without a silica layer. The addition of a layer of silica lowers the ablation threshold. For thicker layers of silica, the ablation threshold rises again.

The first phenomenon can be explained by the lowering of the reflectivity. As apparent from Figure 4.4 the addition of a layer of silica lowers the reflectivity. This must mean the transmission is enhanced. This increase is very small, but since the transmission is very low, it will be a large relative increase. The addition of the silica thus increases the transmitted fluence for a given incident fluence. Therefore a lower incident fluence will suffice to inflict the same damage.

The second phenomenon is a little harder to describe. The presence of the silica not only increases the intensity, it also spatially separates the gold from the surrounding. In order to create a hole, the material needs to be displaced. This will be harder, and hence take more energy, once a thicker silica layers has to be passed.

5 Conclusion & Discussions

5.1 Water

If we calculate the fluence needed to reach the critical density of carriers(see Section 2.4.4), as has been done by Noack et al. [35], we find that this is approximately $0.75\,\mathrm{J\,cm^{-2}}$. We also see that the carrier density depends very strongly on the incident fluence, such that halving the fluence decreases the carriers density by three orders of magnitude. Thus around the maximal fluence reached in this experiment we even expect the reflectivity to drop. This is because the imaginary part of the reflective index has not yet risen enough to compensate for the drop in the real part. This effect is however very small and should be around 2×10^{-4}. This drop should only occur however for the highest fluences since the carrier density is so sensitive for the fluence. Our dataset is not sensitive enough to capture this.

For the medium fluence the Drude-term in the dielectric function is too small to make a significant difference, so we would expect the reflectivity to be constant as a function of fluence. This is also exactly what we see in the data.

A deviation in the theory arises however in the behaviour around $1\,\mathrm{mJ\,cm^{-2}}$. Here we see a sudden rise in reflectivity of 2.3×10^{-3}, which does not match theory. This rise is consistent in that is almost all datapoints with higher fluence agree with the higher value, while almost all the datapoints with lower fluence agree with the lower value. This leads us to think that some process dependant on the carrier density causes this, hence the rapid rise, but that this process is saturated. We can exclude the obvious choice of absorption as the dominant saturated process. The imaginary part of the reflective index is so small, that ignoring this only modifies the reflectivity with 4×10^{-14}.

5.2 Silica on gold

We measured the reflectivity as a function of fluence, for samples consisting of gold with a layer of silica of varying thickness. This drop is gentle in the absence of silica and reasonably gentle for a thickness of $65\,\mathrm{nm}$. The measurements on bare gold overlap almost perfectly with our model. The sample with $65\,\mathrm{nm}$ qualitatively agrees excellent with our model. It quantitatively agrees for low fluences, but the model overestimates the reflectivity for fluences larger then $0.13\,\mathrm{J\,cm^{-2}}$.

For the samples with thicker layers of silica, the measurements only agree qualitatively with our model. Even that agreement is moderate. Here the drop in reflectivity is much less for low fluence then the model predicts. Then, as a certain threshold fluence is reached, the reflectivity drops almost instantly.

33

An expansion of our model, where we assume free electrons from the gold cross an energy barriers to penetrate into the silica, was therefore made. The addition of this process makes the model agree better with the data, since they feature a steeper drop in reflectivity. This agreement is still only qualitatively. The mode does grow three distinctive features, which we also see in our data. These are, as previous mentioned in Section 4.2.3, the relatively weak effect for 65 nm, the strong effect for 115 nm and thicker, and the increase of threshold fluence for thicker layers.

If we look at the ablation threshold we first see the threshold drop at the addition of a silica layer. Also the ablation threshold increases with increasing silica thickness. The first is caused by an increase of the transmittance. We think the second is causes by the increased in energy barrier for the sample to pass in order to leave behind a hole.

6 Acknowledgements

Doing a master research is never something you do on your own. Although my name is the only one on the cover, lots of people have helped in the creation of this work. Here I would like to express my thanks to all these people.

But in order to do that I first need to give you an overview of last year. This project started with an effort of eight people; Robbert Schoo, James Findley-de Regt, Gordian Zomer, Koen Sponselee, Jasper Smits, Qiao Li, Broos Vermeulen and myself. We wanted to break the traditional hierarchic structure of an (assistant-)professor, who supervises a Phd-student, who then supervises a masterstudent. We wanted to form a group, all doing similar research, so we could help each other out, since we were already involved. Over time this deteriorated a bit, since our projects started to drift apart.

During the first four months, the author collaborated with Jasper Clarijs in the creation of an ablation setup for the *Hurricane* laser. This setup and the measurements are discussed by Clarijs [26]. Starting February I supervised a bachelor student: Michiel Bruinewoud. Together we rebuild the setup to connect to the *Mira* laser and performed measurement on water [38]. Between these two constructions every optical element discussed in section 3.1 has been (re)installed. Unfortunately the *Mira* did not perform properly, so we were unable to reach sufficient fluences. This was fixed during the summer break after which the measurement described in this thesis were performed.

As is the tradition, first of all I would like to thank my parents, who brought me to this world and raised me and stimulated me in my youth resulting in me becoming the stubborn and inquisitive person I am today.

The second part of these acknowledgements start with the person who started it all. Robbert Schoo, you were the big motor behind our group project, and even though you hated the term, I still consider you our *primus inter pares*. And during the year you always forced me to understand what I was doing a full 100%(instead of my usual 80%) by persisting in asking off-beat questions and giving off-beat suggestions. And my thanks also go to Peter van de Straten and Dries van Oosten, for actually allowing us to pursue our crazy idea(even though it did not work out in the end). Qiao Li, Koen Sponselee, Jasper Smits and Broos Vermeulen, after our group formation you chose a different route and went to work on Bose-Einstein Condensation, so we had less interaction. Still you contributed a lot in the initial making of the plans and our master student group meetings were always very useful and interesting. And lets not forget the countless number of times you visited our student rooms, making it always crowded and gezellig. Nobody however did more in the preparation phase then James Findley - de Regt. James, I also really valued our discussions about whatever, and I am sorry it usually ended with me insulting your country. The last of the eight, Gordian Zomer, I would like to thank you for your clever little invention to improve

the setup, not to mention the dozens of pieces of software you wrote. And of course the help by working with this and other software, an invaluable help for a computer illiterate like me. I have the feeling you had to explained some things to me three times.

Nothing is more motivating and stimulating then people you collaborate directly with you. The people who stand by you day by day working on the same setup. Those with ideas when you are stuck(and vice versa). Those who make aligning ten times easier and ten times more fun. I need to start with Jasper Clarijs. A partnership formed by accident, which just continued to exist and in the end turned out to be an extremely fruitful one. We took our first steps in experimental research together and I dare say that I would have learned maybe only half as much in these first months without you. And I will never forget the discovery of our alignment in taste of music, especially Billy Joel. In October we were joined by Javier Hernández. Javi, your crash-course on the tricks of laser alignment were a big help. Even in those few weeks, you still managed to create a number of fine anecdotes, such as when you at first thought I was already a PhD-student, or when the plan to take you out to dinner of your last night turned into a large search for you all over Utrecht on a broken bike, ending in your supposed hotel(where they did not know you).

Unfortunately (for me) Jasper left in the Christmas break to continue his research in Davis, California. The hole in my life was quickly filled by Michiel Bruinewoud. Michiel, your project started during a brainstorm of Dries and myself during a talk at the Physics@FOM conference at Veldhoven [43]. So I was involved and enthusiastic about it from the start. Unfortunately you were not able to get great results, but I hope you learned a lot form it and are now more interested in doing experimental physics. I at least had a lot of help from you and I really valued your enthusiasm. And I learned from you how important it is a supervisor to let your students beat you at ping-pong in order to raise their level of confidence. Anne, for the last two months, I was your supervisor. I think neither of us could presume when we stared together in the same mentor group seven years ago we would end up like this. We have not stood in the lab together a lot, but supervising you was always a pleasant break form the dull writing.

Ole Mußman, you became my roommate for the last months, when I was forced to leave my usual quarters. I really liked it, and you were a big help for all the little questions which arise during the writing of a thesis. And I am sorry I distracted you so much by dropping random things out of my hands on the floor, because of my fondness for playing with object and my lack of motor abilities. I think I should also apologize for de-germanizing your lab during our first few months when we used your lab as our personal stockroom(If you are missing a power meter, I probably still have it). But mostly I thank you for your cheerful and kind nature and your tons of (good) suggestions during group meeting, seemingly no matter what the subject was. I really hope you will do something with it and not let your bad experiences lead you astray

from the yellow brick road of academia. Arjon van Lange and Sandy Pratama, thank you for all your small pieces of help during the year and the company during lunches and so. I really enjoyed Sandy's inability to understand the fact that I do not love food as much as he does and Arjons impression of "De vieze man"

The next person to thank is the lab-boss Sebastiaan Greveling. But Sebas, in calling you that way, I am doing you a great disservice, because as lab-boss you mostly told me I had to mop the floor, while you did so much more. Film evenings, swimming outings, almost everything we did as a group which had no link to science originated from you. I am very much looking forward to working with you next years. And there is of course your "subordinate" Karindra Perrier. Karindra, your great skill and joyfulness were always a great inspiration to perform better each day. And thank you for all the love you poured out on us.(I am sorry about your dustbin, lets call it a payback in advance for what you did with my lab coat)

David van der Flier, Charley Beulenkamp, Bart van Assen and Kostas Vourtyras, our research periods overlapped only for a short amount of time. Still I want to thank you for the joy you brought which helped make this section the most fun section in the Ornstein building.

Dante Killian and Frits Diteweg, thank you for all your electronic support, especially when we asked you to make an electronic box we ultimately did not even use. Cees de Kok, we had to tackle a lot of problems with lasers together, and I am sure that without your help, there would not be a working laser left, let alone this master thesis. Paul Jurrius, you also contributed to the setup, but I mostly thank you for the your unstoppable force joy you bring to the group every day.

Andries Lof, I deeply owe you for your help with the characterization of my samples. Without you I still would not have any meaningful results.

And finally Dries van Oosten. You were my supervisor for the entire year, which must have been hard, considering my tendency to burst in your office every other hour. I very much liked our discussions, whether they were about science, politics, science politics or something else. And although you were mostly(for the science part then) right, I will continue to challenge you and be pedantic for the next four years.

Appendix A   Location of measurement fields

In Figures A.1 to A.6 the physical location of each measurement field is shown. In each figure the thick horizontal black line represents the edge of the sample. Since two subsequent shot have a separation of $5\,\mu$m, the size of each field is $50\,\mu$m by $50\,\mu$m. The only exceptions to this are a few field in section 1, which either have less shots, or shots closer together.
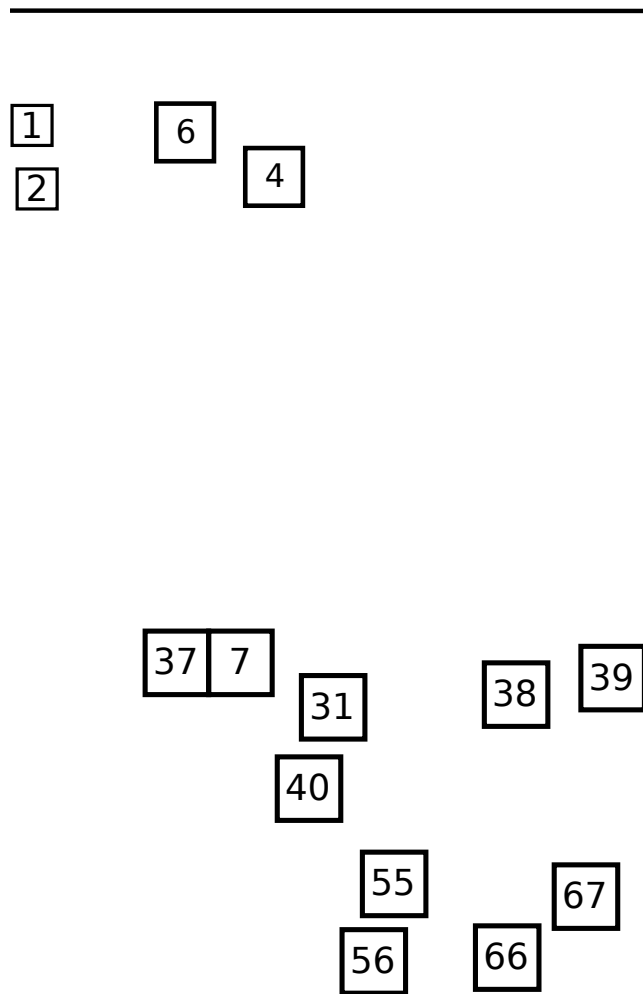
Figure A.1: A schematic overview of location of the measurements in section 1. The thick line indicates the edge of the sample. The size of the large boxes is $50\,\mu m$
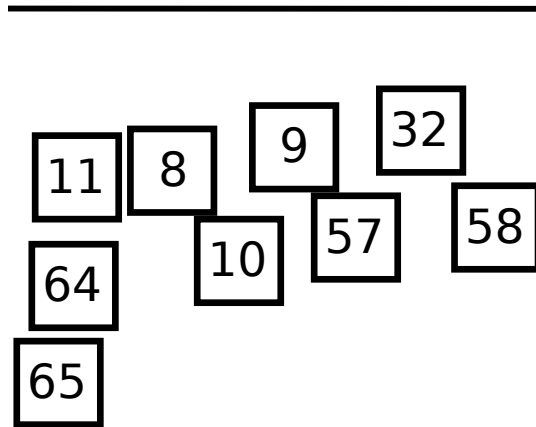
Figure A.2: A schematic overview of location of the measurements in section 2. The thick line indicates the edge of the sample. The size of the boxes is $50\,\mu m$
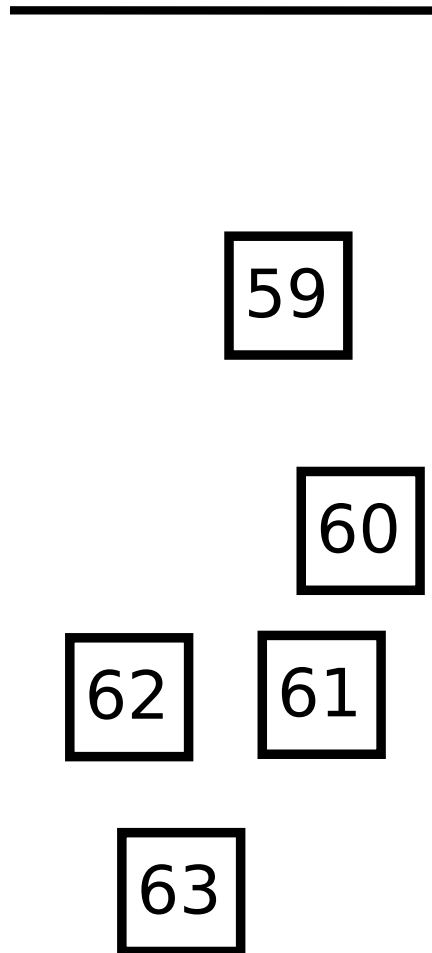
Figure A.3: A schematic overview of location of the measurements in section 3. The thick line indicates the edge of the sample. The size of the boxes is $50\,\mu\mathrm{m}$
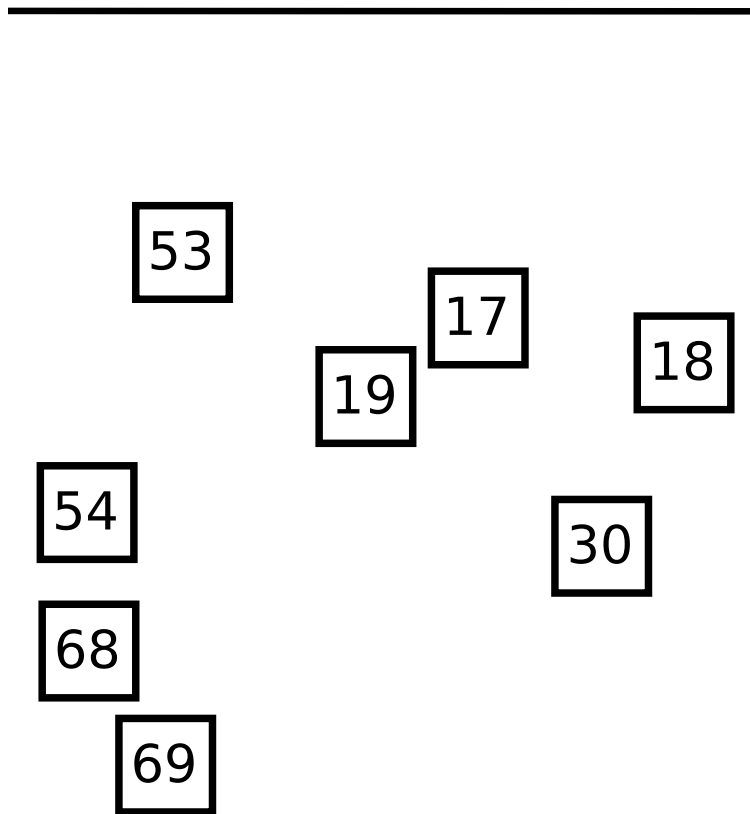
Figure A.4: A schematic overview of location of the measurements in section 4. The thick line indicates the edge of the sample. The size of the boxes is $50\,\mu m$
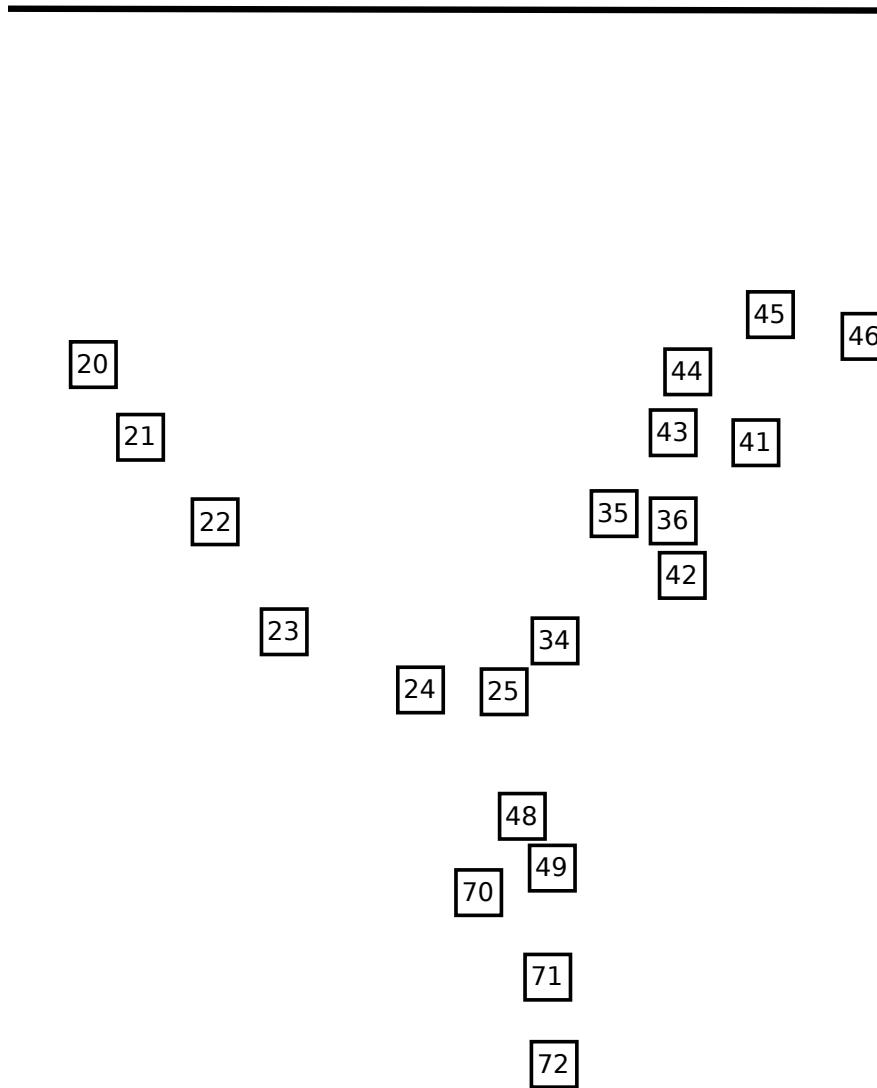
Figure A.5: A schematic overview of location of the measurements in section 5. The thick line indicates the edge of the sample. The size of the boxes is $50\,\mu\mathrm{m}$
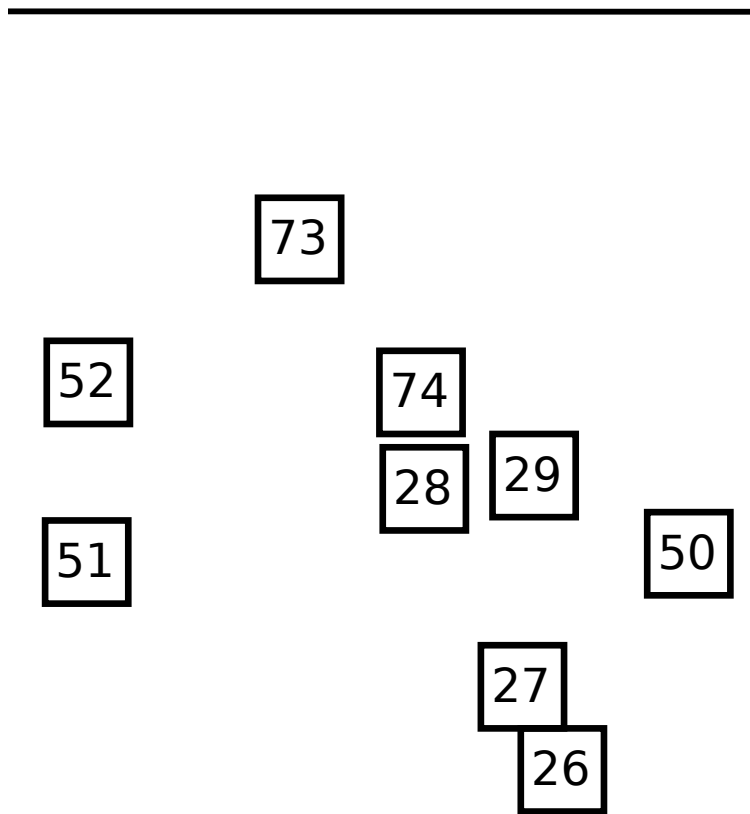
Figure A.6: A schematic overview of location of the measurements in section 6. The thick line indicates the edge of the sample. The size of the boxes is $50\,\mu m$

References

[1] T. H. Maiman, *Optical and microwave-optical experiments in ruby*, Phys. Rev. Lett. **vol. 4**, pp. 564–566 (1960)

[2] E. Archbold and T. Hughes, *Electron temperature in a laser-heated plasma*, Nature **vol. 204**, no. 4959, p. 670 (1964)

[3] S. Penner, *Evavoration coefficients from exposure of a solid to laser radiation*, AIAA Journal **vol. 2**, no. 9, pp. 1664–1666 (1964)

[4] R. G. McKinnell, M. F. Mims, and L. A. Reed, *Laser ablation of maternal chromosomes in eggs of rana pipiens*, Zeitschrift fr Zellforschung und Mikroskopische Anatomie **vol. 93**, no. 1, pp. 30–35 (1968)

[5] A. Pirri, R. Root, and P. S. Wu, *Plasma energy transfer to metal surfaces irradiated by pulsed lasers*, AIAA Journal **vol. 16**, no. 12, pp. 1296–1304 (1978)

[6] C. David, P. Avizonis, H. Weichel, and K. Pyatt, *7a9-density and temperature of a laser induced plasma*, Quantum Electronics, IEEE Journal of **vol. 2**, no. 9, pp. 493–499 (1966)

[7] T. Guo, P. Nikolaev, A. G. Rinzler, D. Tomanek, D. T. Colbert, and R. E. Smalley, *Self-assembly of tubular fullerenes*, The Journal of Physical Chemistry **vol. 99**, no. 27, pp. 10694–10697 (1995)

[8] G. K. Hubler, *Pulsed laser deposition*, MRS Bulletin **vol. 17**, pp. 26–29 (1992)

[9] J. Jia, M. Li, and C. V. Thompson, *Amorphization of silicon by femtosecond laser pulses*, Applied physics letters **vol. 84**, no. 16, pp. 3205–3207 (2004)

[10] H. Zhang, *Single-shot femtosecond laser ablation on the nanoscale*, Ph.D. thesis, Universiteit Utrecht (2013)

[11] S. Preuss, A. Demchuk, and M. Stuke, *Sub-picosecond uv laser ablation of metals*, Applied Physics A **vol. 61**, no. 1, pp. 33–37 (1995)

[12] M. Feuerhake, J.-H. Klein-Wiele, G. Marowsky, and P. Simon, *Dynamic ablation studies of sub-micron gratings on metals with sub-picosecond time resolution*, Applied Physics A: Materials Science & Processing **vol. 67**, no. 5, pp. 603–606 (1998)

[13] M. Li, K. Mori, M. Ishizuka, X. Liu, Y. Sugimoto, N. Ikeda, and K. Asakawa, *Photonic bandpass filter for 1550 nm fabricated by femtosecond direct laser ablation*, Applied Physics Letters **vol. 83**, no. 2, pp. 216–218 (2003)

[14] J. Eizenkop, I. Avrutsky, G. Auner, D. G. Georgiev, and V. Chaudhary, *Single pulse excimer laser nanostructuring of thin silicon films: Nanosharp cones formation and a heat transfer problem*, Journal of applied physics **vol. 101**, no. 9, p. 094301 (2007)

[15] M. Shen, C. Crouch, J. Carey, R. Younkin, E. Mazur, M. Sheehy, and C. Friend, *Formation of regular arrays of silicon microspikes by femtosecond laser irradiation through a mask*, Applied Physics Letters **vol. 82**, no. 11, pp. 1715–1717 (2003)

[16] E. G. Gamaly, S. Juodkazis, K. Nishimura, H. Misawa, B. Luther-Davies, L. Hallo, P. Nicolai, and V. T. Tikhonchuk, *Laser-matter interaction in the bulk of a transparent solid: Confined microexplosion and void formation*, Physical Review B **vol. 73**, no. 21, p. 214101 (2006)

[17] K. Kawamura, T. Ogawa, N. Sarukura, M. Hirano, and H. Hosono, *Fabrication of surface relief gratings on transparent dielectric materials by two-beam holographic method using infrared femtosecond laser pulses*, Applied Physics B **vol. 71**, no. 1, pp. 119–121 (2000)

[18] P. Stampfli and K. H. Bennemann, *Dynamical theory of the laser-induced lattice instability of silicon*, Phys. Rev. B **vol. 46**, pp. 10686–10692 (1992)

[19] C. V. Shank, R. Yen, and C. Hirlimann, *Femtosecond-time-resolved surface structural dynamics of optically excited silicon*, Phys. Rev. Lett. **vol. 51**, pp. 900–902 (1983)

[20] K. Sokolowski-Tinten, J. Bialkowski, and D. von der Linde, *Ultrafast laser-induced order-disorder transitions in semiconductors*, Phys. Rev. B **vol. 51**, pp. 14186–14198 (1995)

[21] A. Rousse, C. Rischel, S. Fourmaux, I. Uschmann, S. Sebban, G. Grillon, P. Balcou, E. Forster, J. Geindre, P. Audebert, J. Gauthier, and D. Hulin, *Non-thermal melting in semiconductors measured at femtosecond resolution*, Nature **vol. 410**, no. 6824, pp. 65–68 (2001)

[22] B. Rethfeld, K. Sokolowski-Tinten, D. von der Linde, and S. Anisimov, *Timescales in the response of materials to femtosecond laser excitation*, Applied Physics A **vol. 79**, no. 4-6, pp. 767–769 (2004)

[23] G. Ramakrishnan, G. K. P. Ramanandan, A. J. L. Adam, M. Xu, N. Kumar, R. W. a. Hendrikx, and P. C. M. Planken, *Enhanced terahertz emission by coherent optical absorption in ultrathin semiconductor films on metals.*, Optics express **vol. 21**, no. 14, pp. 16784–98 (2013)

[24] P. Drude, *Zur elektronentheorie der metalle*, Annalen der Physik **vol. 306**, pp. 566–613 (1900)

[25] M. Born, E. Wolf, A. Bhatia, D. Gabor, A. Stokes, A. Taylor, P. Wayman, and W. Wilcock, *Principles of Optics: Electromagnetic Theory of Propagation, Interference and Diffraction of Light*, Cambridge University Press, seventh ed. (2000)

[26] J. Clarijs, *Femtosecond laser nano-ablation of glass surfaces and their self-scattering effects*, Master's thesis, Universiteit Utrecht (2016)

[27] I. H. Malitson, *Interspecimen comparison of the refractive index of fused silica∗,*, J. Opt. Soc. Am. **vol. 55**, no. 10, pp. 1205–1209 (1965)

[28] C. Fourment, F. Deneuville, D. Descamps, F. Dorchies, S. Petit, O. Peyrusse, B. Holst, and V. Recoules, *Experimental determination of temperature-dependent electron-electron collision frequency in isochorically heated warm dense gold*, Phys. Rev. B **vol. 89**, p. 161110 (2014)

[29] H. Zhang, S. A. Wolbers, D. M. Krol, J. I. Dijkhuis, and D. van Oosten, *Modeling and experiments of self-reflectivity under femtosecond ablation conditions*, J. Opt. Soc. Am. B **vol. 32**, no. 4, pp. 606–616 (2015)

[30] Z. Lin, L. V. Zhigilei, and V. Celli, *Electron-phonon coupling and electron heat capacity of metals under conditions of strong electron-phonon nonequilibrium*, Physical Review B **vol. 77**, no. 7, p. 075133 (2008)

[31] G.Zomer, *Self-scattering of gold nanoparticles under femtosecond ablation conditions*, Master's thesis, Universiteit Utrecht (2016)

[32] F. Williams, S. Varma, and S. Hillenius, *Liquid water as a lone-pair amorphous semiconductor*, The Journal of Chemical Physics **vol. 64**, no. 4, pp. 1549–1554 (1976)

[33] P. K. Kennedy, D. X. Hammer, and B. A. Rockwell, *Laser-induced breakdown in aqueous media*, Progress in Quantum Electronics **vol. 21**, no. 3, pp. 155–248 (1997)

[34] L. Keldysh, *IONIZATION IN THE FIELD OF A STRONG ELECTROMAG-NETIC WAVE*, Jetp, Soviet Physics **vol. 20**, no. 5, pp. 1307–1314 (1965)

[35] J. Noack and a. Vogel, *Laser-induced plasma formation in water at nanosecond to femtosecond time scales: calculation of thresholds, absorption coefficients, and energy density*, IEEE Journal of Quantum Electronics **vol. 35**, no. 8, pp. 1156–1167 (1999)

[36] F. Docchio, *Lifetimes of plasmas induced in liquids and ocular media by single nd: Yag laser pulses of different duration*, EPL (Europhysics Letters) **vol. 6**, no. 5, p. 407 (1988)

References

[37] S. Li, S. Li, S. Anwar, F. Tian, W. Lu, and B. Hou, *Determination of microwave conductivity of electrolyte solutions from debye-drude model*, Session 2A0 p. 657 (2014)

[38] M. Bruinewoud, *Measuring self-reflectivity of a water surface with high-intensity femtosecond laser pulses*, "Bachelor Thesis, Universiteit Utrecht" (2015)

[39] Coherent Laser Group, *The Coherent Mira Model 900 Laser, Operator's Manual* (1991)

[40] APE, *pulseSwitch; Cavity dumper; User manual* (2013)

[41] Andor Technology, *Andor Zyla sCMOS Hardware Guide*, version 1.5 (2014)

[42] G. Hale and M. Querry, *Optical constants of water in the 200-nm to 200-μm wavelength region*, Applied optics **vol. 12**, no. 3, pp. 555–563 (1973)

[43] J.-P. Delville, *Light moves liquid*, physics@FOM conference (2015)